



Multi-stage sulfide evolution of the Moran Ni sulfide ore, Kambalda, Western Australia: insights into the dynamics of ore forming processes of komatiite-hosted deposits

Sebastian Staude¹ · Marcus Oelze² · Gregor Markl¹

Received: 26 August 2020 / Accepted: 24 May 2021 / Published online: 5 October 2021
© The Author(s) 2021

Abstract

The Moran komatiite-hosted Ni sulfide deposit at Kambalda (Australia) is one of the better preserved orebodies at Kambalda. Its geochemical signature is used to investigate the evolution of the sulfide mineralization. The orebody has several parts, including a flanking segment where massive sulfides formed relatively early and a central portion in a 40-m-deep erosional embayment representing a later generation of massive and net-textured sulfides. Basal massive sulfides within the deep embayment vary systematically in their chalcophile element contents (Ni, PGE, Au, Te, As, Bi). Elements compatible in monosulfide solid solution (MSS) exhibit the highest concentration at the edge of the orebody (up to 4.3 ppm Ir + Os + Ru + Rh), whereas incompatible elements are most concentrated in the centre (up to 11.2 ppm Pt + Pd + Au). This difference in element distributions is explained by fractional crystallization of sulfide melt from the edge towards the centre. To explain the vertical movement of the residual fractionated melt, a new model of sulfide crystallization is proposed. A low-viscosity boundary layer containing incompatible elements is formed between MSS and sulfide melt. This melt propagates with the crystallization front towards the centre of the sulfide melt pool. Trace element variations in pentlandite (e.g. Co) and composite Co- and Bi-bearing arsenide-telluride grains suggest that during the final stages of crystallization, an immiscible Co-As-Te-Bi melt is formed.

Keywords Kambalda · Komatiite · Magmatic sulfides · Sulfide fractionation · Boundary melt layer · Sulfide trace elements

Introduction

Archaean komatiite-hosted Ni-Cu-Co sulfide deposits are an important source for sulfide Ni (Gole and Barnes 2020). The East Yilgarn komatiite Ni province is the third largest Ni producer in the world after Sudbury and Noril'sk (Hronsky and Schodde 2006; Naldrett 2010). The Yilgarn deposits are always metamorphically and tectonically overprinted to various degrees, and igneous textures in sulfides are commonly modified or destroyed (Barnes et al. 1988a, b; Barnes 2006a, b). This is contrary to many mafic intrusion-hosted sulfide deposits where igneous textures in sulfides tend to be better

preserved (e.g. pentlandite loops around pyrrhotite; see below) (Barnes et al. 2020).

The crystallization of magmatic sulfides starts with the formation of Fe-rich Ni-bearing monosulfide solid solution (MSS) at high temperatures (1150 °C) (Naldrett 2004), whereas Cu remains in the melt. The behaviour of Ni is dependent on the sulfide melt composition and the temperature. At temperatures around 1100 °C, Ni is mildly incompatible in MSS, whereas at 900 °C, it is mildly compatible (Barnes et al. 1997). Below 870 °C, high-form pentlandite becomes stable, and due to the peritectic reaction of MSS with the remaining Ni-bearing melt (Kitakaze et al. 2016; Mansur et al. 2019), pentlandite loops form around MSS (now pyrrhotite), referred to as loop texture (Barnes et al. 2020). The Cu-rich portion of the melt forms intermediate solid solution (ISS; now chalcopyrite). Therefore, pentlandite can be regarded as a magmatic phase, and trace elements in pentlandite can be used for deciphering petrogenetic processes during crystallization of magmatic sulfide melts. Platinum-group elements (PGEs) together with other

Editorial handling: W. D. Maier

✉ Sebastian Staude
sebastian.staude@uni-tuebingen.de

¹ Department of Geosciences, University of Tübingen, Schnarrenbergstrasse 94-96, 72076 Tübingen, Germany

² GFZ German Research Center for Geosciences, 14473 Telegrafenberg, Germany

trace elements can serve as recorders of fractional crystallization processes (e.g. Barnes and Ripley 2016, and references therein). Osmium, Ru, Ir and Rh are compatible into MSS, whereas Pt, Pd, Au, Te, Sb, Bi and As remain in the melt (Mungall et al. 2005; Helmy et al. 2010; Dare et al. 2014; Liu and Brenan 2015; Barnes and Ripley 2016; Duran et al. 2017).

There are many systematic studies of the entire orebodies in Cu-bearing mafic systems showing fractional crystallization trends over various size scales, where Cu-rich sulfide bodies form during advanced crystallization (e.g. Naldrett et al. 1996; Duran et al. 2017; Lightfoot 2017; Mao et al. 2019; Mansur et al. 2020; Tolstykh et al. 2020; Járóka et al. 2021). Fewer deposit-scale studies are available on the Cu-poor komatiite-hosted massive sulfide deposits. This is most likely due to the lack and limited accessibility of intact orebodies in the komatiite systems. Perring (2015) provided drill hole data of the komatiite-hosted Cliffs deposit in Western Australia (WA) showing systematic variation in Ni across the orebody. This was interpreted to represent variation in R factor (silicate melt:sulfide melt mass ratio) during channelled flow with variable degrees of melting and entrainment of underlying older sulfides. No other geochemical data were provided, and thus, few constraints exist with regard to sulfide liquid crystallization or fractionation.

Barnes (2004) documented extensive fractionation of the PGEs in the Silver Swan orebody at Black Swan (WA). Keays et al. (1981) found systematic variations in PGE tenors (tenor is the metal content in 100% sulfides) in Kambalda ores but interpreted them to be due to hydrothermal remobilization. Tenor variations of Ni were observed in the Wannaway deposit (WA) (Seat et al. 2004) and the Edwards Lode (Kambalda, WA) (Heath et al. 2001) and were attributed to structural and metamorphic processes. The variability of PGEs attributable to sulfide liquid fractionation has also been recognized at Alexo in the Abitibi belt (Canada) (Barnes and Naldrett 1986), Perseverance-Agnew (Barnes et al. 1988b) and Emily Ann (Barnes and Liu 2012) in the Eastern Goldfields (WA). Lightfoot et al. (2017) documented wide variability in sulfide tenor in the intrusive komatiite-hosted Thompson deposit (Manitoba, Canada); this deposit has been extensively tectonized under granulite facies conditions, and Lightfoot et al. (2017) interpreted the variability to be due to differential migration of solid sulfide during deformation.

The Moran komatiite-hosted sulfide deposit in Kambalda (WA) is favourable for the study of systematic variations in sulfide composition as the deposit is not deformed or dismembered by younger tectonic activity. Many igneous textures are preserved in the sulfides and surrounding lithologies despite the metamorphic overprint (Staude et al. 2016, 2017a, 2020, 2021; Barnes et al. 2018). Staude et al. (2017a) showed that the onset of sulfide ore formation

caused enhanced thermal erosion of the underlying older rocks as a result of the high density and very low viscosity of the sulfide melt as well as the hydrated nature of the substrate. In most cases, erosion resulted in elliptical embayments at the bottom of the lava channel. The margins of the channel are marked by undercut features called pinchouts, completely surrounding the embayment. In these pinchouts, massive sulfides are bound by older rocks both underneath and above, suggesting that the sulfide melt thermally erodes sideways (Staude et al. 2016). These data suggest that the orebodies have formed from a homogeneous sulfide melt pool overlain by a network of sulfide melt between olivine crystals. Due to the relatively minor nature of the metamorphic overprint, the geochemistry of the orebody potentially preserves signals of its magmatic origin and evolution, including sulfide liquid fractional crystallization trends.

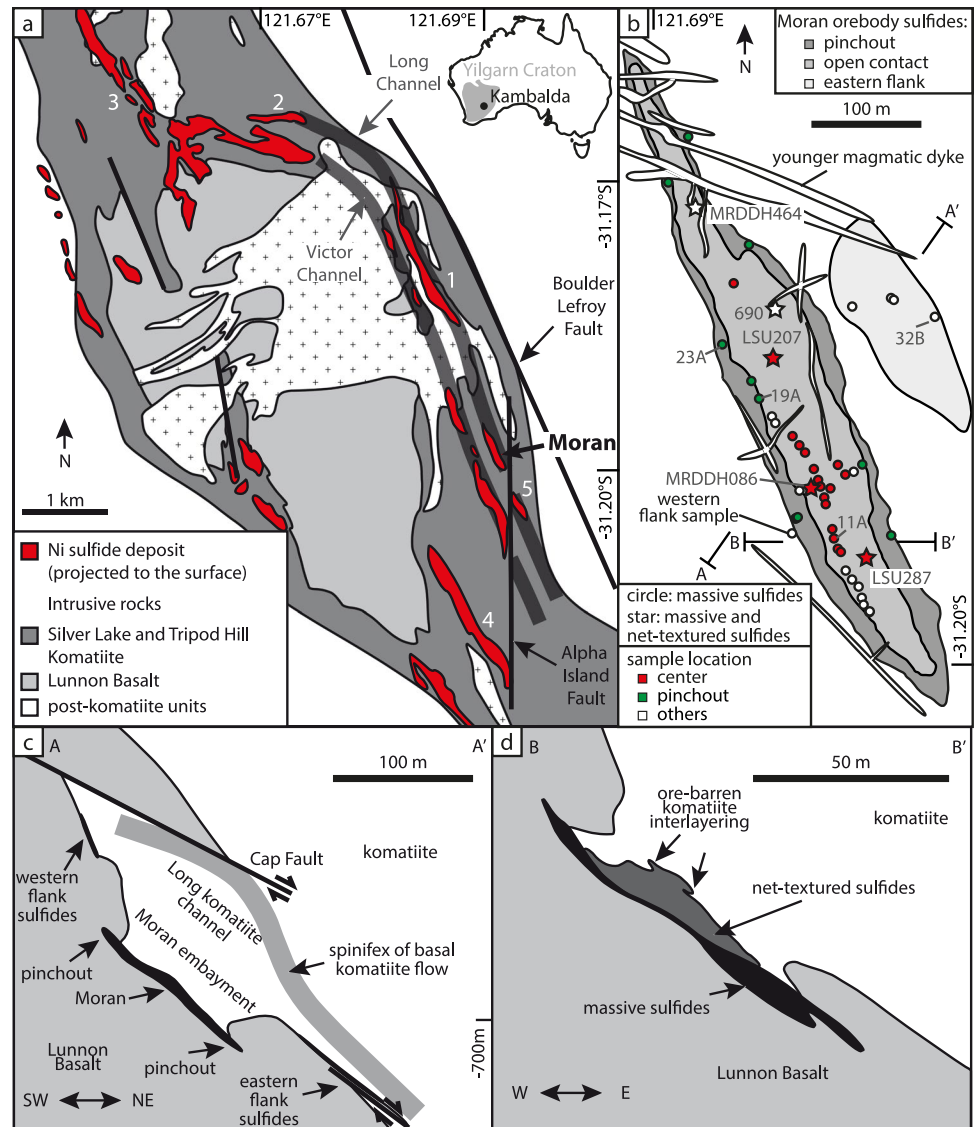
In this study, we investigate geochemical variations over the Moran orebody and consider how this variation resulted from the crystallization of Cu-poor sulfide melt pools. Geochemical differences between massive sulfides and net-textured sulfides are also discussed with implications for the formation of net-textured sulfides.

Geology

Overview of the Kambalda geology

Magmatic rocks of the Kambalda Dome (Fig. 1) are part of the 2.7 Ga old Kalgoorlie Terrane of the Yilgarn Craton (WA) (Gresham and Loftus-Hills 1981; Goscombe et al. 2009). The succession starts with the tholeiitic Lunnon Basalt, which is overlain by up to 10 m of mafic to siliceous sediments (Bavinton 1981; Gresham and Loftus-Hills 1981; Beresford and Cas 2001) that contain sulfides (mostly pyrrhotite, minor chalcopyrite and sphalerite). The sediments are overlain by lava flows of the Silver Lake Member of the Kambalda Komatiite. The sediments and part of the uppermost Lunnon Basalt are eroded by the Silver Lake Komatiite notably where the basal lava flow is channelized (Gresham and Loftus-Hills 1981; Leshner 1989; Staude et al. 2017a). The resulting embayments host the Ni sulfide deposits of Kambalda typically at the base of a thick olivine cumulate pile. In non-channelized areas, the contact sediments are preserved and overlain by several thin komatiite flows of the sheet-flow facies (Gresham and Loftus-Hills 1981; Barnes 2006b; Gole and Barnes 2020). The Silver Lake Komatiite Member is overlain by lava flows of the Tripod Hill Komatiite, which generally lack sulfides (Gresham and Loftus-Hills 1981; Thomson 1989). Several more volcanic and sedimentary units (i.e. Devon Consols Basalt, Kapai Slate, Paringa Basalt, Black Flag Group) (Said

Fig. 1 **a** Simplified geological map of the Kambalda Dome showing the location of Moran on the eastern limb of the dome. Other deposits mentioned in the text are Long (1), Durkin North (2), Juan (3), Lunnon (4) and Moran South (5). The dark grey lava channels of Long and Victor represent the approximate area of the sediment-free window between the basalt and komatiite. Outline of the Yilgarn Craton in the inset from Goscombe et al. (2009). **b** Map of the main Moran orebody (pinchout and open contact both within the embayment) and its eastern flank sulfides, the location of the pinchout and younger magmatic dykes, as well as the sample locations (dot, massive sulfide samples; star, massive sulfide and net-textured ore samples). **c** Profile A-A' of **b** showing the Moran embayment with flanking sulfides and the spinifex-textured top of the Long channel lava flow. Note, sulfides in the centre represent massive and net-textured sulfides. **d** Profile B-B' of **b** highlighting the distribution of massive and net-textured sulfides within the embayment. Note the interlayering of net-textured ore and barren komatiite in the upper portion of net-textured ore



and Kerrich 2010) were deposited on top of the komatiites. Subsequently, the whole stratigraphy was intruded by mafic to felsic dykes, sills and intrusive bodies and metamorphosed to upper greenschist to lower amphibolite facies (Gresham and Loftus-Hills 1981). Despite the metamorphism, igneous textures are locally preserved (Gresham and Loftus-Hills 1981; Groves et al. 1986; Thomson 1989; Staude et al. 2016, 2017a, 2020, 2021; Staude and Markl 2019; Barnes et al. 2018). Accordingly, the prefix “meta” is omitted.

Geology of the Moran deposit

The Moran orebody is situated on the eastern limb of the Kambalda Dome in the same channel that hosts the Durkin North and Long orebodies to the north and the Moran South mineralization to the south (Barnes et al. 2013; Staude

et al. 2017b). The orebody is one of the better preserved in the Kambalda Dome area, with no large faults and only thin younger magmatic dykes cutting it (Fig. 1b). The thickness of the first komatiite flow overlying the Moran orebody is ~90 m in the centre of the embayment but a mere ~10 m along the flanks of the lava channel (Fig. 1c).

The elliptical Moran embayment is about 660 m long and varies between 50 and 120 m in width (Fig. 1b–d). It is up to 40 m deep as a result of thermomechanical erosion by the sulfide melt (Staude et al. 2017a). The erosion also operates sideways during embayment formation, creating a pinchout of sulfides that intruded the basalt (Staude et al. 2016). The pinchout completely surrounds the orebody and extends between 5 and 25 m into the basalt (Fig. 1b–d). Massive sulfides (>90% sulfide content) measure up to 4 m in thickness in the pinchout, whereas they amount to a mere 20 cm in the centre of the orebody. The contact of the massive sulfides

to the older basalt is an outstanding example of a sulfide-silicate melting-infiltration front (Barnes et al. 2018), characterized by an assemblage of remarkably well-preserved igneous textures: (1) undulating basal contacts with sulfide-filled micro-fractures and ferrichromite layers, (2) basalt-sulfide breccia-emulsions and basalt plumes on basal contacts, (3) basalt-sulfide emulsions on basal and upper pinchout contacts and (4) cm-scale silicate-sulfide layering and a floating vesicular basalt “scum layer” on the upper pinchout contacts. These originate from the thermomechanical erosion of the basalt by the sulfide liquid (Groves et al. 1986; Staude et al. 2016, 2017a).

In the main central part of the embayment, away from the marginal pinchouts, a thin layer of massive sulfides is overlain by net-textured sulfides (also called matrix sulfides) (Barnes et al. 2017), where sulfides form a network around the former (now serpentinized) olivine cumulate framework. In contrast to other deposits at Kambalda and elsewhere (i.e. O’Toole, Brazil; Brenner et al. 1990; Alexo and Raglan, Canada; Leshner 2007; Houlié et al. 2012), two layers of net-textured sulfides exist in the Moran deposit (Fig. 2). The basal layer (net-textured sulfide layer I) is in direct contact with underlying massive sulfides and reaches a thickness of 3 m in central areas, diminishing towards the pinchout. The second layer of net-textured sulfides (net-textured sulfide layer II) is separated from the first layer by a 30–50-cm-thick planar layer of barren komatiite (Fig. 2). Net-textured sulfide layer II is also thickest (up to 5 m) in the central area and thins towards the pinchout; however, some interlayering with barren komatiite is observed (Fig. 1d). Layer II also shows an internal layering on the cm-scale due to variable proportions of sulfides, whereas net-textured sulfide layer I is mostly homogeneous, except in the upper 6–8 cm.

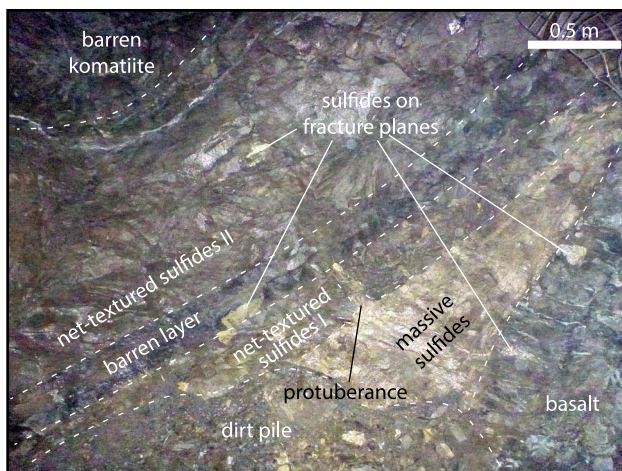


Fig. 2 Underground photo of Moran sulfides highlighting the two layers of net-textured sulfides on top of massive sulfides

A thin massive sulfide body measuring about 200 m in length along the channel and 80 m across is preserved on the flank of the Moran embayment (Fig. 1b, c). Close to the centre of the embayment, the sulfides are situated directly on top of the Lunnon Basalt, whereas farther away, they overly the sediments. Igneous textures are preserved along the base of the sulfide body as molten sediment-sulfide melt emulsions (Staude et al. 2017a). Most of the flanking sulfides do not have net-textured sulfides above them, except within 10–20 m to the embayment, where up to 30 cm of net-textured ore is present.

Sampling and sample description

Samples have been collected from drill core and underground development (Fig. 1b). Samples of massive sulfides were collected every 10 m along a profile from the margin to the centre of the Moran orebody, with two to seven samples across the thickness of the sulfide body at each position. Additional samples were taken from other areas to cover the whole orebody systematically, including flank sulfides. Samples from the basalt-sulfide contact usually show the igneous textures described above, whereas other massive sulfide samples exhibit a foliation of pentlandite and pyrrhotite caused by metamorphism. Rarely, loop textures are preserved (pentlandite surrounding pyrrhotite grains) (Barnes et al. 2020; Fig. 3a). Locally developed metamorphic porphyroblasts, composed of pyrite-chalcopyrite symplectite up to 20 cm in size, were avoided in sampling, although on a microscopic-scale, minor amounts of the symplectite are found in all samples.

Besides pyrrhotite, pentlandite and chalcopyrite, magnetite is common in massive sulfides from the main orebody forming large crystals up to 100 μm diameter or large anhedral aggregates up to 1 mm. In contrast, magnetite is rare in sulfides from the flanks. Skeletal chromite is found on the contact of massive sulfides with basalt and net-textured sulfides, respectively (Ewers and Hudson 1972; Staude et al. 2017a). Pentlandite occurs mostly as mm-sized irregular aggregates and bands and rarely as μm -sized exsolution aggregates (flames) in pyrrhotite. Anhedral aggregates of mm-sized sphalerite have been observed in samples from the flanks only. Arsenides and tellurides are commonly observed but only in very small quantities. Arsenides comprise euhedral sperrylite ($< 20 \mu\text{m}$), which is typically overgrown by a euhedral sulfarsenide (Fe-bearing gersdorffite-cobaltite solid solution, similar to the magmatic sulfarsenides described by Le Vaillant et al. (2018)) of up to 100 μm size (Fig. 3b). The most abundant telluride is anhedral spherical Pd-bearing melonite usually overgrowing the arsenides and less commonly altaite in addition to undetermined Ag-Te and Bi-Te phases. These composite arsenide-telluride aggregates

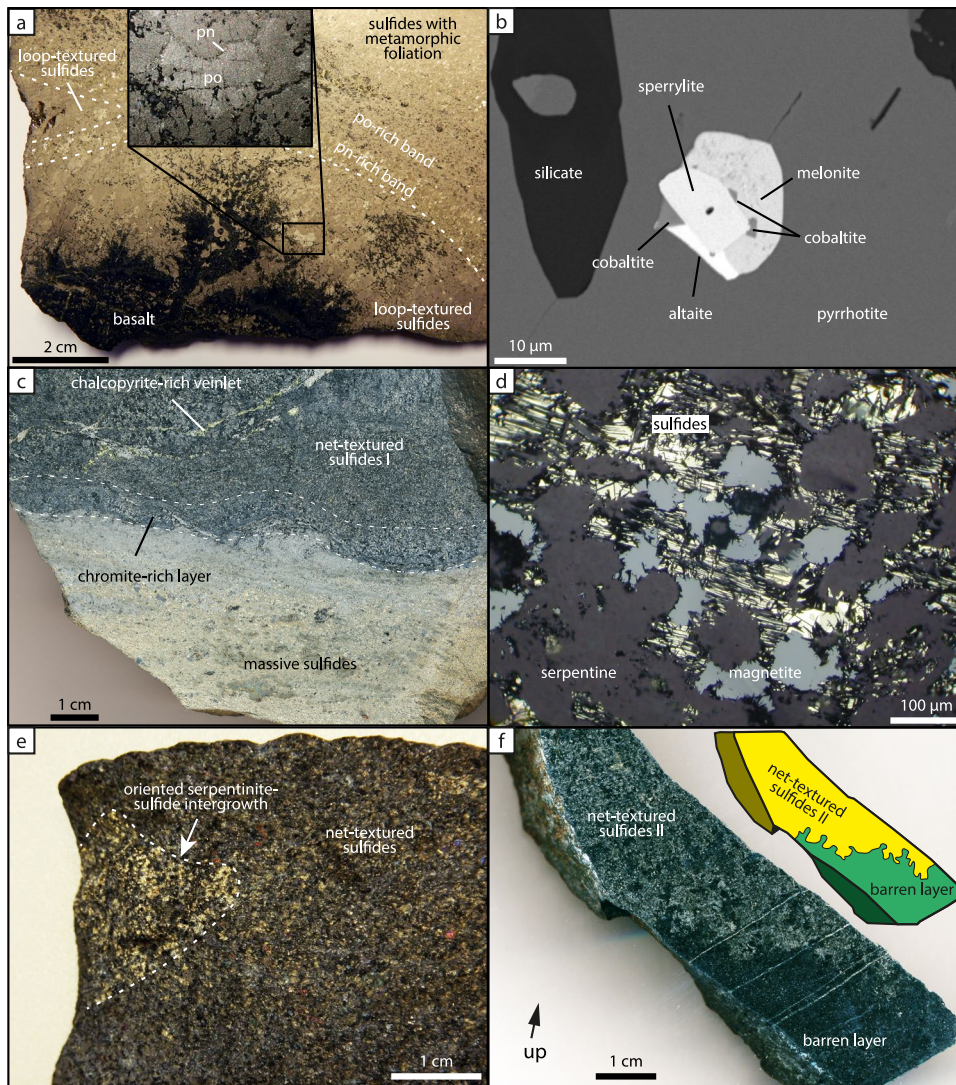


Fig. 3 **a** Photo of polished hand specimen with typical contact between basalt and massive sulfides. In proximity to the base of the sulfide layer, relic loop textures are preserved, whereas the remaining sulfides are foliated. The inset shows a pyrrhotite (po) grain which is completely surrounded by a <math><1\text{ mm}</math>-sized pentlandite (pn) loop. A chemical map of this sample showing the loop texture is presented in Barnes et al. (2020). **b** BSE image of composite grain of euhedral arsenides (sperrylite, cobaltite) overgrown by anhedral tellurides (melonite, altaite) from a massive sulfide sample. Black spot in sperrylite is a void. **c** Photo of polished hand specimen of the massive sulfide contact to the overlying net-textured ore I. The contact zone

contains a high chromite content. Also note the chalcopyrite veinlet in net-textured ore. **d** Photomicrograph in reflected light in air of net-textured sulfides showing relic cumulate texture of former olivine (now serpentine). **e** Hand specimen of typical net-textured sulfides with patches where the light reflects on parallel cleavage surface of the sulfides (oriented serpentinite-sulfide intergrowth). This is interpreted to reflect former monosulfide solid solution crystals. **f** Polished hand specimen and accompanying sketch of the contact between the barren komatiite layer and the net-textured ore II above. Note the cauliflower-like texture of the contact

(Fig. 3b) are rare in samples from the pinchout (not in every thin section), whereas in the centre of the Moran deposit, up to 20 grains were observed in one thin section.

Net-textured sulfides were sampled in 5 profiles along the orebody (stars in Fig. 1b). The contact of massive to net-textured sulfides is sharp but undulating (Fig. 3c). The primary texture of all net-textured sulfides (layers I and II) is destroyed by randomly oriented serpentine blades cutting through the sulfides, although in rare cases, round

sulfide-free areas resemble former olivine grains (Fig. 3d). Many samples show an oriented intergrowth of serpentine and sulfides, which is visible when light is reflected homogeneously in up to 3 cm large areas (Fig. 3e). Net-textured sulfide layer I is terminated by an increasing amount of patchy silicate over a distance of 6–8 cm. Layer II starts with a sharp downward-facing cauliflower-like texture (Fig. 3f), whereas its upward termination is similar to layer I.

All net-textured samples contain pyrrhotite, pentlandite and chalcopyrite and large amounts (about 10 vol.% based on digital image processing) of magnetite. Arsenides or tellurides have been observed only in rare cases in net-textured samples. Chromite, overgrown and partially replaced by magnetite, is common in samples from layer I and in the barren layer, although rare in layer II.

Methods

Whole-rock major and trace elements

The samples analysed in the present study comprise massive sulfides (mostly 50–100 g) and net-textured sulfides (mostly 200–300 g) (Fig. 1b). Major and trace elements including PGE and Au were determined at Bureau Veritas (Perth, WA). Samples were digested using 4-acid digestion or peroxide fusion, respectively. Parts of the samples were decomposed using a Leco furnace for S analysis by infrared spectroscopy, and 40 g were used for fire assay to determine the PGE and Au content using Ni sulfide to collect the precious metals. Analysis was carried out using ICP-AES or ICP-MS, respectively (see electronic

supplementary material (ESM) 1 for digestion and analytical methods used). Multiple standards and blanks were dispatched in addition to the laboratory repeats, standards and blanks to check for precision and accuracy (ESM 2). Representative results are listed in Table 1. Selected elements and element ratios are plotted in ESM 3. All whole-rock analyses were recalculated to 100% sulfides using the method of Barnes and Ripley (2016) to allow internal comparison.

Major element composition of sulfides determined by electron microprobe analysis (EMPA)

The sulfide major element chemistry was determined using a JEOL 8900 electron microprobe at the University of Tübingen (Germany). Analyses were carried out in wavelength-dispersive (WD) mode using an acceleration voltage of 25 kV, a probe current of 20 nA with a focused beam and PRZ correction. Counting times on the peak position (all $K\alpha$) were 15 s for main elements (Cu, Ni, Fe, S) and 30 s for trace elements (Se, Bi, As, Co). Representative results are presented in Table 1, and all results in wt% and atoms per formula unit are provided in ESM 1.

Table 1 Representative samples of whole-rock massive sulfides and electron microprobe and LA-ICP-MS analyses of the selected sulfides in massive sulfides from various locations of the orebody. All data is found in ESM 1

		Flank sulfides on sediments	Pinchout sulfides	Transitional sulfides	Central sulfides
Sample		32B	23A	19A	11A
Whole rock (tenor in ppm)	Ni	62800	145700	176700	203600
	Co	1700	1920	2110	562
	Ir+Os+Ru+Rh	1.42	1.04	2.13	900
	Pt+Pd+Au	0.11	0.77	13	5170
	Te+As+Bi+Sb	2.2	34	25	71
Pyrrhotite EMPA (wt%)	Fe	59.0	59.3	59.4	59.3
	Ni	0.50	0.51	0.51	0.51
	S	39.8	39.6	40.0	39.8
	Co	0.07	0.07	0.06	0.07
Chalcopyrite EMPA (wt%)	Fe	30.1	30.1	30.3	n.a.
	Cu	34.9	35.0	34.9	n.a.
	S	35.7	35.8	35.1	n.a.
	Co	0.04	0.04	0.02	n.a.
Pentlandite EMPA (wt%)	Fe	29.4	29.9	29.5	30.4
	Ni	36.1	35.8	36.1	36.0
	S	33.5	33.1	32.8	33.4
	Co	1.10	0.43	0.51	0.14
Pentlandite LA-ICP-MS (ppm)	Co	9660	4010	4250	880
	Te	2.30	7.30	15.7	18.3
	Pd	0.17	1.49	0.25	2.49

n.a. not analysed

Trace element analyses of sulfides by LA-ICP-MS

Laser ablation analysis was carried out using the Analyte Excite 193 nm excimer laser (Teledyne Photon Machines, Bozeman, MT, USA), coupled to the quadrupole-ICP-MS iCAP from Thermo Scientific at the GFZ (Potsdam, Germany). The LA system is equipped with a HelEx II 2-volume ablation cell. Helium was used as a carrier gas for aerosol transport from the sample surface to the ICP and was mixed downstream with Ar as a make-up gas before entering the plasma. Operational parameters of the ICP-MS instrument and LA unit were tuned for maximum sensitivity, low oxide formation based on the $^{232}\text{Th}^{16}\text{O}/^{232}\text{Th}$ ratio and low laser-induced elemental fractionation based on the $^{232}\text{U}/^{232}\text{Th}$ ratio using NIST SRM 610. Quantitative analyses of samples were performed by ablating 40- μm spots with a laser repetition rate of 10 Hz with a beam energy at the sample of $\sim 2\text{--}3\text{ J/cm}^2$. A total of 24 elements were analysed at each spot. The analysis time for each sample was 50 s, with 20 s for measurement of the baseline with gas background (laser off) and 30 s of signal analysis with laser on. The following isotopes were measured ^{34}S , ^{57}Fe , ^{59}Co , ^{60}Ni , ^{63}Cu , ^{66}Zn , ^{75}As , ^{77}Se , ^{101}Ru , ^{103}Rh , ^{108}Pd , ^{107}Ag , ^{111}Cd , ^{118}Sn , ^{121}Sb , ^{125}Te , ^{182}W , ^{185}Re , ^{189}Os , ^{193}Ir , ^{195}Pt , ^{197}Au , ^{208}Pb and ^{209}Bi . The measurements were performed by using a multi-standard approach where the samples were bracketed by two different external calibrators. We measured PGE-FeS (Wohlgemuth-Ueberwasser et al. 2007) for Ru, Rh, Pd, Re, Os, Ir and Pt. All other elements have been calibrated using MASS-1 (USGS; Wilson et al. 2002).

We also analysed as standard the doped artificial sulfide UQAC-FeSB (see provisional values in ESM 1). Standards were inserted after every 10 analyses of unknowns. Iron was used as internal standard, its content being based on independent EMPA determinations from the same areas of interest. Time intervals for data reduction were selected by visual inspection of each spectrum using Iolite™ a package for Igor Pro™ (Paton et al. 2011). We do not apply interference correction for Ni on ^{101}Ru or Cu correction on ^{103}Rh because we obtain the correct reported values for the known–unknown material which contains 2.5 wt% Ni and 2.3 wt% Cu. Based on these measurements, we do not report ^{101}Ru values for samples with a Ni content higher than 2.5 wt% nor ^{103}Rh values for samples with Cu content higher than 2.3 wt%. The reported ^{108}Pd values are corrected for the ^{108}Cd interference using the approach reported in Sylvester (2001). Uncertainty estimates for the elements measured are based on repeated measurement of the reference material UQAC-FeSB. Representative results are presented in Table 1 with the complete set of the results given in ESM 1 and selected elements plotted in ESM 3.

Two-dimensional X-ray imaging

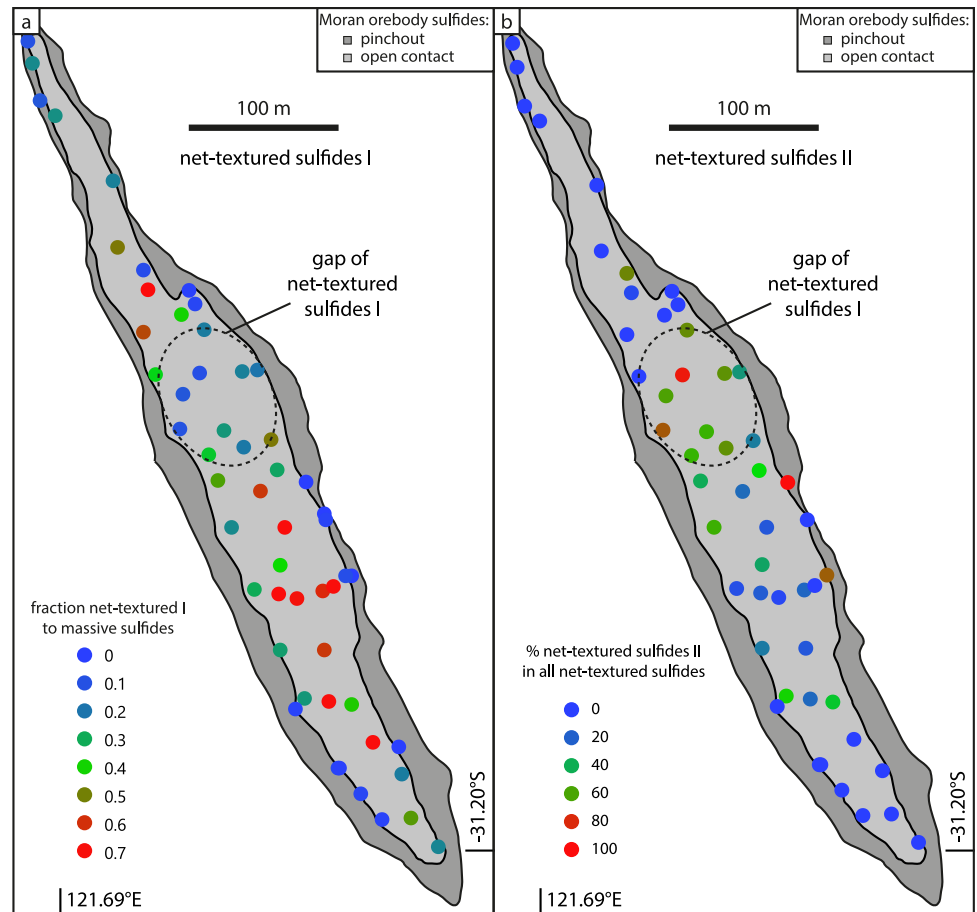
Qualitative element distribution maps were acquired at CSIRO, Melbourne (Australia), using the Maia Mapper, a high definition μXRF element mapping system developed for the analysis of large samples (Ryan et al. 2018). The Maia Mapper comprises (i) a Maia 384-element X-ray detector (Kirkham et al. 2010), (ii) a high brightness MetalJet D2 liquid metal micro-focus X-ray source from Excillum AB [3], (iii) an efficient polycapillary X-ray lens producing a focus on target of $\sim 30\ \mu\text{m}$ and (iv) a high-precision, high-speed sample positioning mechanical system that presents samples up to $500 \times 150\ \text{mm}^2$ in size and 10 kg in weight to the beam focus in a “fly scan” continuous raster. Data is acquired continuously as individual photon events tagged with sensor number and X, Y position. Image “pixels” are reconstructed from the X, Y with an effective dwell time in each pixel set by the motion velocity. Data reduction is performed using the GeoPIXETM software, which uses a standardless fundamental parameter method. The data is analysed event by event using the dynamic analysis (DA) method for real-time spectral deconvolution to accumulate element concentration maps with spectral overlap, pileup and background removed (Ryan et al. 2014). X-ray fluorescence microscopy images are presented as combinations of normalized element maps (scale stretched between minimum and maximum pixels) with a different element in each of the red, green and blue channels scaled to the maximum concentration and combined into a single 24-bit colour image. Images were collected with a spot size of 25 microns, pixel size 25 microns and a dwell time of 10 ms per pixel.

Results

Proportion of net-textured to massive ore

The Moran drill hole database of IGO Limited (now owned by Mincor Resources LN) was used to estimate the relative proportion of massive and net-textured sulfides. The amount of sulfides in basal sulfide-matrix breccia ore was added to massive sulfides as the breccia sulfides represent part of the massive sulfide pool (Barnes et al. 2018). The sulfur content of sulfide-matrix breccia and net-textured ore was used to calculate the amount of sulfides within the specific drill interval. The overall distribution of net-textured sulfides I and II, based on this drill hole information, is shown in Fig. 4. Layer I is thickest in the southern portion of the central area (coinciding with the thinnest part of massive sulfides). Layer II is thickest in the northern portion of the central area.

Fig. 4 Distribution of net-textured sulfides, based on drill hole information, shown as the ratio of thickness of net-textured sulfides I and II to the thickness of immediately underlying massive ore. **a** Fraction of net-textured sulfide I. Note the lower amount of net-textured sulfides in the upper central part of the orebody. **b** Fraction of net-textured sulfide II. Note the higher fraction of net-textured sulfides in the same area where layer I is thinner



Whole-rock major and trace element chemistry: massive sulfides

Whole-rock major and trace element contents vary systematically across the orebody. The Ni tenor increases in flank sulfides from 6 wt% farthest away from the Moran embayment to 12 wt% closest to the embayment. The Ni tenor in the main orebody varies from 8 to 20 wt% in the pinchout to up to 28 wt% in the centre. Additionally, only in the centre, the Ni tenor shows a large variation from 10 to 28 wt%. Such large variations are not observed for any trace elements. Trace elements are grouped based on their partitioning behaviour into MSS: IPGE and Rh are compatible with regard to MSS, whereas Pt, Pd, Au and Cu are incompatible. The IPGE + Rh show the highest concentration in the pinchout with a combined tenor up to 4.3 ppm, whereas Pt, Pd and Au have their highest concentration in the centre with a combined tenor up to 11.2 ppm (Fig. 5a, b). A variation similar to Pt, Pd and Au is observed for Te (Fig. 5c), Bi, As, Zn and Mo (Fig. 5; ESM 1). No systematic variation of IPGE + Rh content is observed on the flanks. In contrast, combined Pt, Pd and Au contents show an increase towards the embayment reaching up to 4 ppm.

Whole-rock major and trace element chemistry: net-textured sulfides

Major and trace element tenors of net-textured sulfides differ from the tenors of the massive sulfides. A variation in metal content is also visible between net-textured ore layers I and II and also within a single layer at different locations of the orebody (ESM 4). The Ni tenor in the basal net-textured layer I is typically slightly higher compared to massive sulfides underneath. There is little variation within layer I where it is thin, but where it reaches several metre thicknesses (MRDDH086), compositional variation is evident. The Ni tenor decreases from around 20 wt% where the net-textured sulfides overlie massive sulfides to around 15 wt% at the contact with the barren layer above (ESM 4). The Ni tenor of the net-textured ore II shows no systematic lateral variation within the layer. However, within individual vertical profiles, a variation is visible. Whereas Ni in net-textured ore I is decreasing upwards, it is increasing upwards in net-textured ore II (ESM 4).

The concentrations of the IPGE + Rh are slightly lower in the basal net-textured ore I, with a combined average grade of 800 ppb, compared to massive sulfides underneath

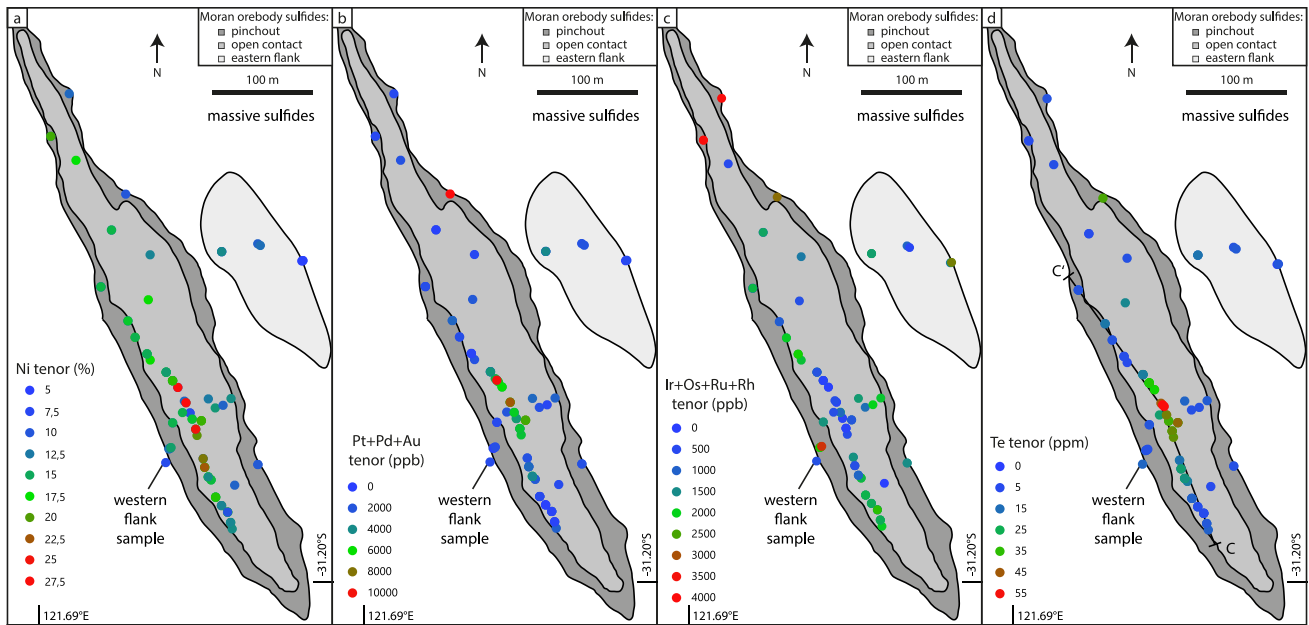


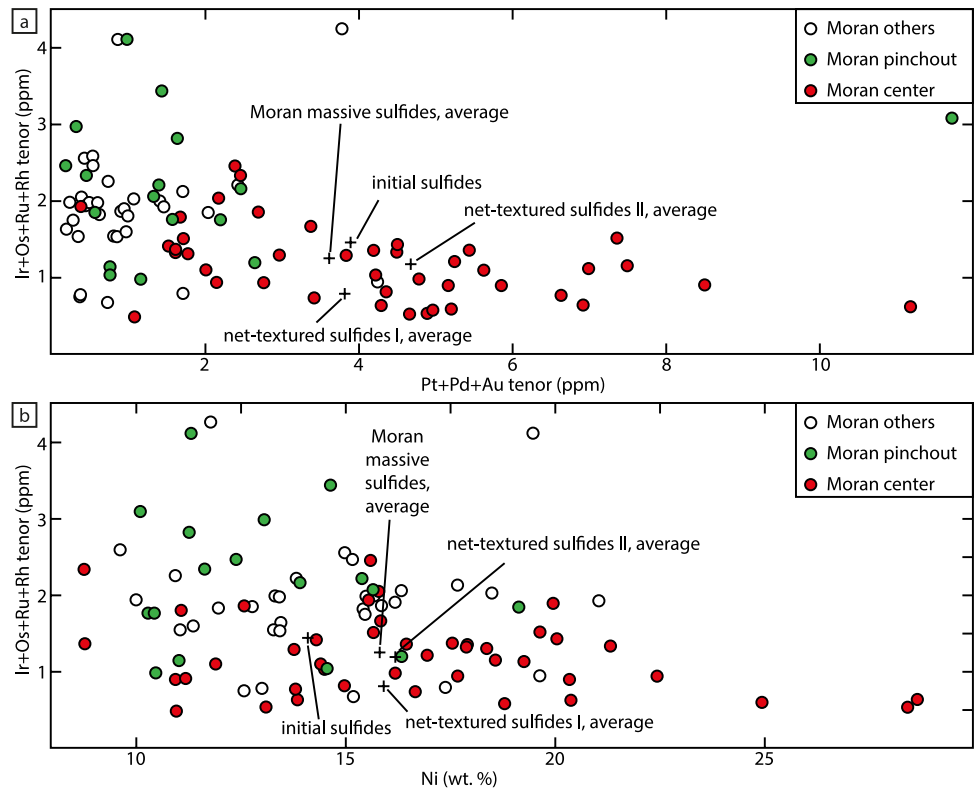
Fig. 5 Maps of Moran showing the tenor (metal content in 100% sulfides for whole-rock data) of selected chalcophile elements. **a** Ni tenor for massive sulfide samples. **b** Combined tenor of Pt, Pd and Au

for massive sulfide samples. **c** Combined Ir, Os, Ru and Rh tenor for massive sulfide samples. **d** Tellurium tenor for massive sulfide samples. Profile C–C’ is shown in Fig. 7

with 1300 to 1900 ppm (MRDDH086). In contrast, Pt, Pd and Au are higher in net-textured ore I with an average of 2960 ppb compared to the underlying massive ore with 1960 to 2000 ppb. Both IPGE + Rh and combined Pt, Pd and Au

contents vary between individual drill holes of the same ore type (ESM 4). An IPGE + Rh versus Pt, Pd and Au plot and an IPGE + Rh versus Ni plot are shown in Fig. 6. The average of all data of net-textured ore layers I and II show that

Fig. 6 Combined tenors of Ir, Os, Ru and Rh plotted versus combined tenors of Pt, Pd and Au (**a**) and versus Ni (**b**) for massive sulfide samples. Shown are also the calculated initial sulfide composition, the average massive sulfides and the average of net-textured layers I and II. Colours as in Figs. 1b and 11a



their composition approaches that of the average massive sulfides (half of the Moran profile C–C' to cover a section from the pinchout to the centre).

Chromium shows an interesting behaviour that reflects the chromite content of the sample. From net-textured layer I towards the barren layer, it increases to up to 2500 ppm and drops sharply down to 500 ppm on the contact to net-textured layer II (ESM 5). Within the net-textured layer II, the chromite content increases again to up to 2000 ppm with stratigraphic height over the barren layer. Other major and trace elements show no systematic variation in net-textured sulfides.

Sulfide mineral chemistry of massive sulfides

Whereas pyrrhotite and chalcopyrite show no systematic spatial variation of major or trace elements (Table 1, ESM 1), pentlandite shows some significant variations in massive sulfides. The molar Fe/Ni ratio increases from 0.84 in the pinchout to 0.92 in the centre, although the overall Ni tenor of the whole rock increases towards the centre. The Pd content of pentlandite is relatively low at the margin (0.1–2 ppm) but up to 11 ppm in the centre. The only other trace element in pentlandite showing systematic variations

is Co. The highest Co content (up to 1 wt%) was found in pentlandite from the flank situated on footwall sediments. Pentlandite from flank sulfides overlying basalt and most pentlandite from the main orebody contain between 4000 and 5500 ppm Co without any systematic variation. In the central part of the Moran orebody, however, the Co concentration in pentlandite drops within a very short lateral distance (metres to a few tens of metres) down to 200 ppm (Fig. 7a, b). These are the same samples that show the highest Pt, Pd, Au and Te concentrations (Fig. 7c), although there is no systematic variation of Te in pentlandite. No systematic variation in major or trace elements of pentlandite has been observed in net-textured samples.

Two-dimensional X-ray imaging

Chemical variations of sulfides within net-textured sulfides I and II, and between both types, cannot be shown using X-ray imaging due to the small grain size of the sulfides and silicates. However, the technique is ideal to highlight certain textural observations. Net-textured layer I is homogeneous with an even distribution of Cu, Fe and Ni. Only the upper 6–8 cm of the layer shows a patchy distribution of sulfides with a sharp contact between the homogeneous and

Fig. 7 **a** Map of Moran showing the distribution of the Co content in pentlandite. **b** Co content of pentlandite along profile C–C' profile. **c** Combined Te, Bi, As and Sb tenor of massive sulfides along the same C–C' profile. Note the strong decrease of Co in pentlandite in the centre of the deposit, marked by the red lines in (a) to (c), concomitant with a strong Te + Bi + As + Sb tenor increase. Error bars in **b** are the estimated 10% measurement uncertainty based on the intermediate precision of the used secondary reference material UQAC-FeSB

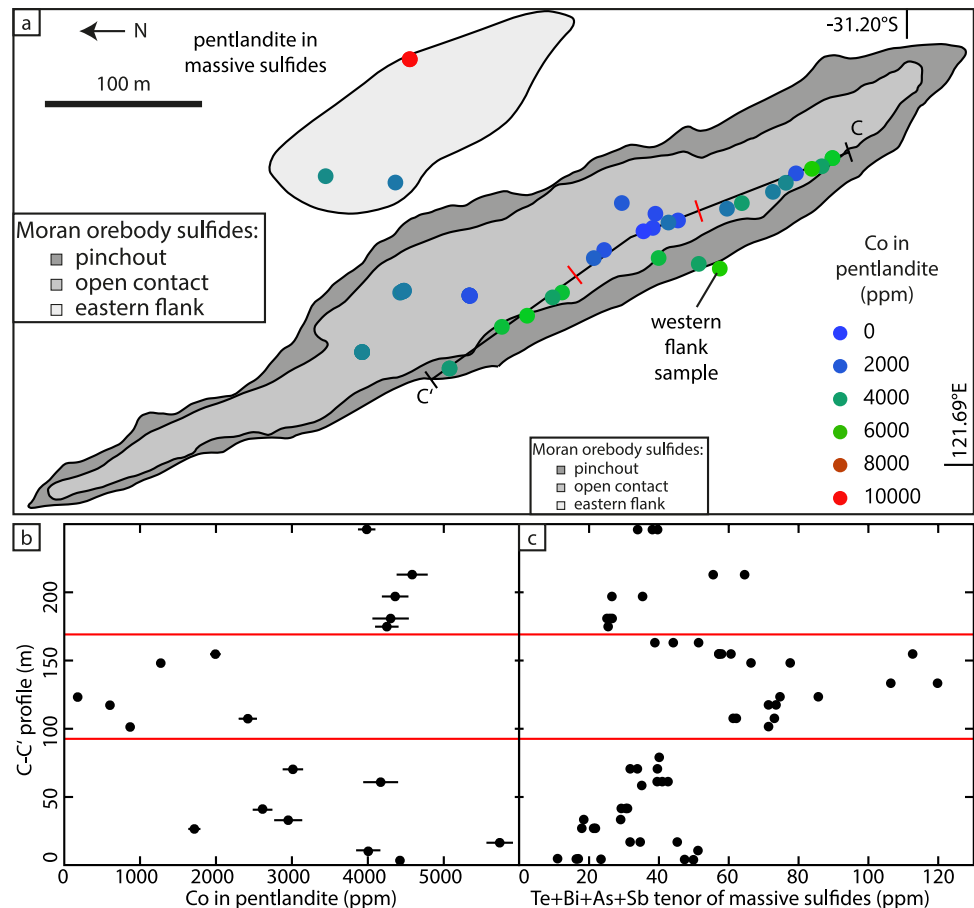
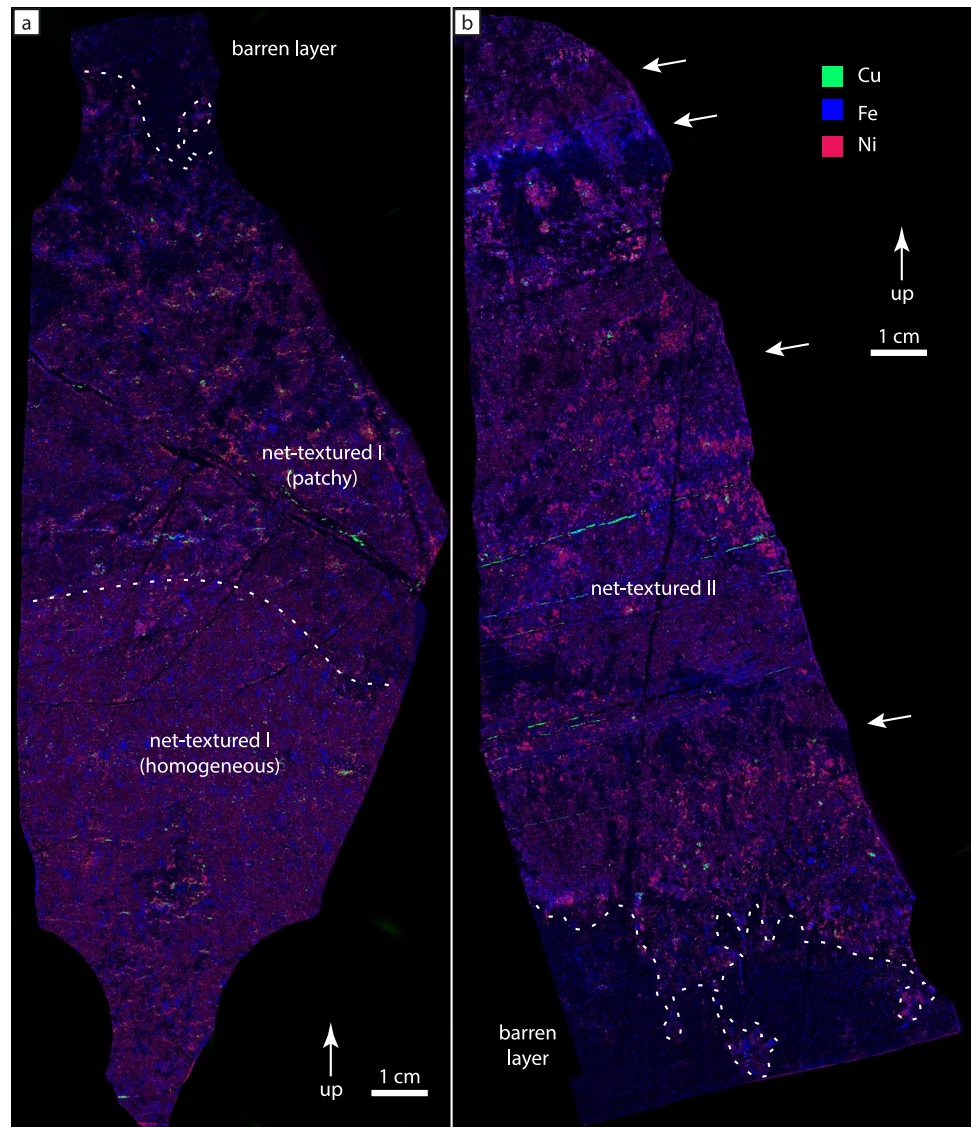


Fig. 8 False-colour chemical maps of Cu, Fe and Ni of polished slabs of net-textured ore I (**a**) and II (**b**). Note the sharp contact between homogenous and patchy net-textured sulfides in the upper part of the net-textured layer I and the horizontal layering in net-textured sulfide II (highlighted with arrows) which is missing in net-textured sulfide I. Contacts between textures are highlighted in white



the patchy part (Fig. 8). The contact to the overlying barren layer is sharp. Net-textured layer II shows a patchy distribution of sulfide containing sulfide-poor areas that are interlayered with sulfide-rich areas (Fig. 8). The distribution of Cu (mainly in fractures) and Ni is more irregular compared to the upper layer of net-textured sulfide I.

Discussion

Effect of metamorphism and alteration

The presence of pentlandite-pyrrhotite foliation in massive sulfides (Fig. 3a) and symplectitic chalcopyrite-pyrite intergrowths reflects an overprint of deformation and metamorphism. Nevertheless, the observed chemical and mineralogical variations in the Moran orebody are

interpreted to reflect predominantly magmatic processes during their formation, for the following reasons. (1) Delicate basalt plumes represent frozen igneous textures on the basal sulfide contact (Staudé et al. 2016, 2017a). (2) The whole-rock chemistry of basalt plume samples (recalculated to 100% sulfides) is identical to foliated samples from the same sampling site. These data suggest that metamorphism did not cause significant chemical modification of the sulfides and that pentlandite was remobilized by ductile flow in solid state rather than by dissolution and redeposition. (3) The observed composite arsenide-telluride grains are similar in texture to those found at other (unmetamorphosed) magmatic deposits (Piispanen and Tarkian 1984; Garuti and Rinaldi 1986; Dare et al. 2014). (4) In addition, simulations of fractionation of Moran sulfides largely reproduce the observed whole-rock trends.

Sulfide evolution in the Moran embayment

The origin of the embayments and pinchouts at the base of the Kambalda lava flows have been intensely discussed in the literature. These structures have been interpreted to be features resulting from thermomechanical erosion (Huppert and Sparks 1985), structurally formed by folding or thrusting (Stone and Archibald 2004; Stone et al. 2005), synvolcanic graben faulting (Brown et al. 1999) or pre-volcanic topography (Gresham and Loftus-Hills 1981; Squire et al. 1998) potentially modified by thermomechanical erosion (Leshner et al. 1984; Williams et al. 1998). Tenor variations of Ni within a single orebody have also been attributed to structural or metamorphic processes (Heath et al. 2001; Seat et al. 2004). Textural evidence from the contacts between older Lunnon Basalt and younger sulfides of the Moran deposit, including basalt melt plumes and emulsions, suggest that the embayment and the pinchout of Moran were formed by thermomechanical erosion (Staude et al. 2016, 2017a). The erosion created an early wide and concave embayment and later on a narrower evolved steep-sided and deep embayment surrounded by a late pinchout (Fig. 1c, d) overprinting the early concave embayment.

Massive sulfides are found on the flanks and at the base of the embayment and are interpreted to have different histories. Flank sulfides are formed at an early stage in a wide concave embayment with the sulfides farthest away from Moran being the oldest (Staude et al. 2017a), whereas the main sulfide melt pool is formed subsequently within the main lava channel whose floor was being simultaneously deepened by erosion (Fig. 9a, b). Therefore, once the steep-sided embayment is formed, the flank sulfides were not in contact anymore with the sulfide melt pool on the base of that embayment and were not susceptible of subsequent upgrading by ongoing komatiite lava flow. In contrast, the sulfide pool within the embayment continued to interact with flowing komatiite lava. Thus, the geochemistry of the massive sulfides on the flanks and the main orebody reflect two principally different formation mechanisms. The flank sulfides preserved their original composition, varying laterally with distance from the embayment. This can be seen in the Ni and trace element data, which gradually increase towards the embayment (Fig. 5, ESM 3). This reflects increasing degrees of equilibration between the sediment-derived sulfide and komatiite lava and hence increasing silicate melt:sulfide melt mass ratio R (R factor). There are several publications dealing with the variations in trace elements between flank and channel environment and the gradual upgrading by ongoing replenished lava flows (e.g. Leshner and Campbell 1993; Leshner and Burnham 2001; Leshner et al. 2001; Barnes et al. 2013). They show that the chalcophile metal content of the sulfide melt increases with longer flow durations and higher flow rates, which is reflected in

the geochemical data from the flanks. The main orebody, on the other hand, represents an initially well-equilibrated, homogeneous sulfide melt pool that was shielded from further interaction with the lava once the net-textured sulfide zone had developed above it. This sulfide pool then evolved as a nearly closed system during solidification as further explained in the following sections.

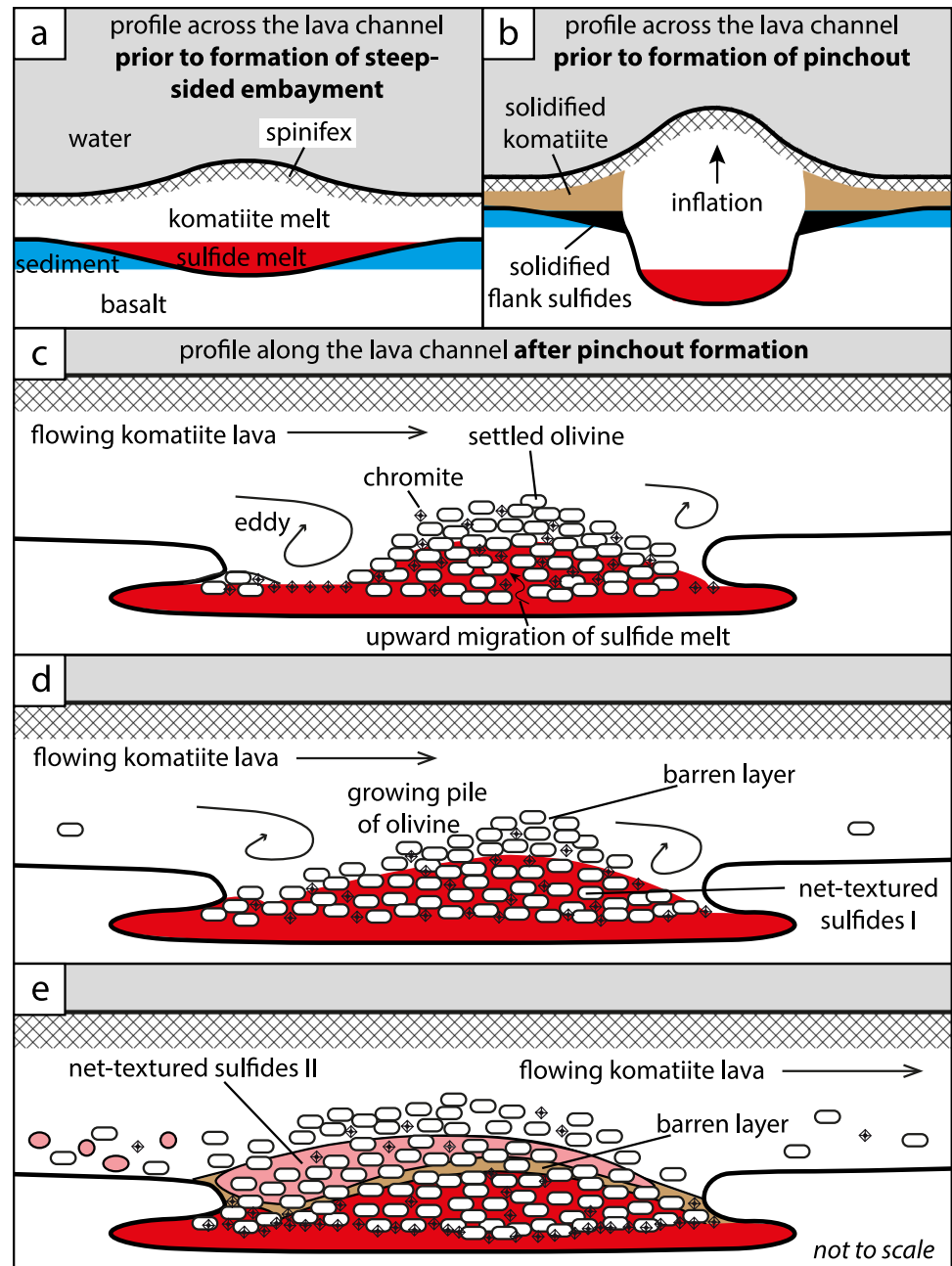
Once the lava flow ceased, olivine settled to form the net-textured sulfides on top of the massive sulfides. The absence of any significant net-textured sulfide I in the northern part of Moran (Fig. 4) is interpreted to reflect the specific magma flow dynamics: assuming a southward flow direction (Staude et al. 2017b), the laminar flowing lava could have formed eddies at the margin of the embayment (Barnes and Robertson; Fig. 9c). The turbulent convection in the eddy kept any olivine phenocrysts in suspension, whereas in the centre of the embayment where magma flow was less turbulent, the entrained olivine crystals precipitated. The settled olivine then partially sank into the top of the sulfide melt pool (driven by the balance of positive buoyancy of olivine in sulfide and negative buoyancy in the komatiite melt) forming net-textured sulfides (Naldrett 1973). The pile of olivine and resulting net-textured sulfides is thicker in less dynamic portions of the lava channel, explaining the distribution of net-textured sulfides I (Figs. 4 and 9d).

Continued cooling and settling of olivine were accompanied by (at least partial) solidification of interstitial silicate melt limiting the amount of olivine submerging into the sulfide melt, leaving a layer of barren olivine cumulate above net-textured layer I. This presence of a barren silicate layer between net-textured layers I and II shows that net-textured layer I cannot have formed by sulfide infiltration from above (Barnes et al. 2017). This observation instead favours the “billiard ball model” where olivine submerges into the sulfide melt (Naldrett 1973).

In contrast, the net-textured layer II is suggested to have formed by downward sulfide percolation as suggested by the downward-facing cauliflower-like morphology of its basal contact (Figs. 3f and 8b) and the patchiness of the sulfide distribution and presence of cm-scale sulfide free domains (Fig. 8b), a hallmark of channelized percolation (Barnes et al. 2017). The thickest accumulation of net-textured sulfides II is located where the first layer is thinnest because further sulfide and olivine bearing komatiite mush filled the topographic lows of the underlying cumulate pile. This subsequent magma pulse could have formed by re-entrainment of previously deposited sulfide possibly from the Long deposit upstream (Barnes and Robertson 2019).

The spatial variation of chromite in net-textured sulfides provides additional information on the cooling history. Prior to any silicate crystallization, skeletal chromite is formed underneath the basal sulfide melt by reaction of the sulfide melt with re-melted basalt (Fig. 10) (Staude

Fig. 9 Cartoon illustrating the formation of massive and net-textured ores I and II of the Moran orebody and explaining their spatial distribution. **a** Profile across the lava channel during the initial stages of embayment formation creating a concave embayment. **b** Flank sulfides and komatiite are cut-off from the lava flow and solidify during the formation of the steep-sided embayment while the flow is inflating. **c** Profile along the lava channel. Chromite, derived from the melting of the basal basalt (Staude et al. 2016, 2017a), floats to the upper contact of the massive sulfide pool due to its intermediate density. Once the eruption ceases and/or lava cools, olivine crystallizes and settles. Eddies form at the edges of the embayment preventing olivine from settling in this position and causing the olivine crystal pile to be thicker in the centre of the channel (Robertson and Kerr 2012). The basal net-textured layer forms by partial sinking of olivine cumulates into the sulfide (“billiard ball model” of Naldrett 1973). **d** Continued settling of olivine along with cooling of the system causes interstitial silicate melt to (at least partly) crystallize preventing further submergence of olivine and thus forming a barren layer on top of net-textured ore I. **e** A new pulse of sulfide- and olivine-rich lava is deposited on top of this barren layer forming net-textured ore II. See text for further explanation



et al. 2016, 2017a). This chromite is buoyant due to the trapped silicate inclusions in its skeletal parts and concentrates at the contact between the sulfide melt and komatiite melt (Staude et al. 2017a). This horizon is ultimately transformed to the net-textured sulfide I. Chromite at the contact of massive to net-textured ore (Fig. 3c) has also been observed in other komatiite-hosted sulfide deposits in WA (several occurrences are summarized in Groves et al. 1977) and elsewhere (e.g. Abitibi, Canada, Houlié et al. 2012). Olivine crystals sinking through the komatiite and into the top of the massive sulfide incorporate the rising chromite crystals. As long as the footwall basalt is

above its melting temperature, chromite continues to form and ascend and can be trapped underneath the net-textured sulfides (Fig. 10), forming a chromite layer also observed in other komatiite-hosted deposits. In the initial net-textured layer II, no chromite occurs as chromite grains are unable to migrate into this layer due to the sealing barren layer and because the overlying komatiite flow is not cool enough yet to crystallize chromite. During the formation of the second layer of net-textured ore, cooling continues and reaches the crystallization temperature of chromite, which explains the increasing chromite content from the barren layer towards the top of net-textured layer II (ESM 5).

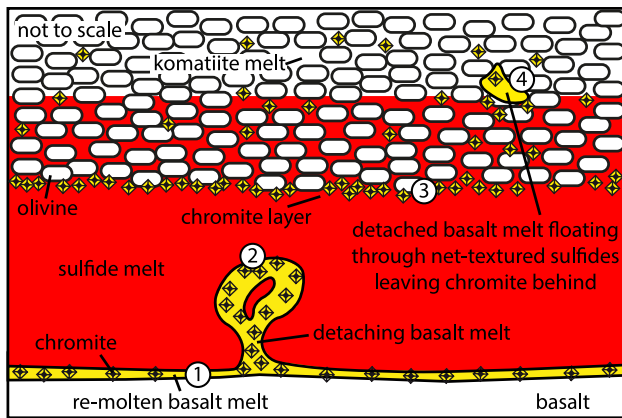


Fig. 10 Sketch of chromite occurrences in Moran sulfides. Melting of the footwall basalt results in crystallization of skeletal chromite (1). Once the melt film becomes too thick, it forms a plume and detaches, floating with the chromite through the sulfide melt (2). Chromite is concentrated along the contact between massive sulfide and net-textured sulfide (3). Basalt melt rising through the cumulate pile can also deposit chromite within the net-textured sulfides (4)

Effect of sulfide crystallization and fractionation on geochemistry

Modelling fractional crystallization of sulfide melt

In order to model the crystallization of the sulfide melt, the initial composition of the sulfide melt needs to be known. The average Ni tenor calculated through half of the Moran profile C–C' covering a section from the pinchout to the centre is 16 wt%. The partition coefficient for Ni between sulfide melt and silicate melt is dependent on the melt composition and temperature. We used the komatiite Ni and FeO data presented by Barnes et al. (2013) from channel spinifex samples, representing background values. At temperatures between 1500 and 1600 °C, the Ni partition coefficient varies from 400 to 500 (Kiseeva and Wood 2015). Thus, we used an average value of 450 for further calculations. An R factor of 200 results in an initial Ni content of the sulfide melt of 14 wt%, which is close to the observed Ni tenor. An R factor of 200 was thus used to calculate the trace element content of the initial sulfide composition; additional calculations with R factors of 400 and 600 were performed for Pd and Ir to study the influence of variable R factors.

The initial concentration of an element in the sulfide melt was used to calculate fractionation trends using the Rayleigh fractionation equation:

$$C_L = C_0 \times F^{(D-1)} \quad (1)$$

$$C_S = C_L \times C_0 \times F^{(D-1)} \quad (2)$$

In these equations, C_L is the concentration of the element in the fractionating sulfide melt, C_0 the initial concentration of an element in the sulfide melt quantified above, F the fraction of the melt, D the partition coefficient between the MSS and sulfide melt and C_S the concentration in the crystallizing MSS. The partition coefficient (Table 2) is dependent on temperature, melt composition and other factors (Mungall et al. 2005). Results of the calculations are shown in Table 2 and Fig. 11.

Calculations for most elements reproduce the trends observed at Moran; hence, it is proposed that the orebody most likely cooled and crystallized from the pinchout (early MSS cumulates) towards the centre (remaining fractionated melt). Palladium, for example, is calculated to be between 150 and 200 ppb in the first MSS (Table 2), which is the range observed in the pinchout of Moran (ESM 1). The modelling predicts that the concentration of Pd in the last 20–30% of the remaining melt should be between 5000 and 7000 ppb, which is consistent with observations from the centre of Moran. Elements with low D (<0.1) increase drastically in their concentration in the melt during the last stage of crystallization. Tellurium, for example, more than doubles in the sulfide melt between 70 and 90% crystallization (Table 2), which is also observed in the centre of Moran (Fig. 7).

Implications for the crystallization history of Moran massive sulfides

The modelling in the previous section shows that the concentration of trace elements in the Moran sulfides is consistent with fractional crystallization. This crystallization proceeded from the pinchout towards the centre crystallizing first MSS and then ISS. Mantle-normalized Rh/Pt ratios have been used in the past to identify MSS cumulates in massive sulfides due to the preferred incorporation of Rh into MSS (Barnes et al. 1997; Barnes 2004). Accordingly, a map of Moran with mantle-normalized Rh/Pd (Pd instead of Pt is used to avoid analytical nugget effects) (Barnes, unpublished data) is shown in Fig. 12. The map highlights that in most parts of Moran mantle-normalized Rh/Pd is relatively high (>2), and therefore, a large proportion of Moran can be assumed to consist of MSS cumulates. In the centre of the deposit, the mantle-normalized Rh/Pd is locally relatively low. Based on digital imaging, this area represents about 15% of the surface area, and combining it with profiles across (i.e. Fig. 2d) and along the embayment (Staude et al. 2017a), the sulfide volume in this area represents less than 1% of the initial sulfide melt pool. The massive sulfides are only about 20 cm in thickness in this domain (compared to 4 m in the pinchout). This area is characterized by the highest concentrations of incompatible elements (Figs. 5 and 12), the thinnest massive sulfides and

Table 2 Fractional crystallization calculations of selected elements. See text for more information

	Pd		Te		Ir		Rh	
$C_{\text{komatiite}} \text{ (ppb)}$	8.5 ¹		200 ⁴		1 ¹		1.2 ¹	
$D_{\text{sulfide melt/silicate melt}}$	57000 ²		4500 ²		48000 ²		25000 ²	
$D_{\text{MSS/sulfide melt}}$	0.09 ³		0.03 ⁵		2 ⁶		2 ⁶	
	C_L^{Pd}	C_S^{Pd} (ppb)	C_L^{Te} (ppb)	C_S^{Te} (ppb)	C_L^{Ir} (ppb)	C_S^{Ir} (ppb)	C_L^{Rh} (ppb)	C_S^{Rh} (ppb)
$C_{\text{sulfide melt}}$ (ppb)	1700		40,000		200		250	
F=0.9	1900	170	44,000	1300	180	360	225	450
F=0.8	2100	190	50,000	1500	160	320	200	400
F=0.7	2400	210	57,000	1700	140	280	175	350
F=0.6	2700	240	65,700	2000	120	240	150	300
F=0.5	3200	290	78,000	2400	100	200	125	250
F=0.4	3900	350	97,000	2900	80	160	100	200
F=0.3	5100	460	129,000	3900	60	120	75	150
F=0.2	7400	660	191,000	5700	40	80	50	100
F=0.1	13,900	1240	373,000	11,200	20	40	25	50

$C_{\text{komatiite}}$ concentration of element in komatiite melt, $D_{\text{sulfide melt/silicate melt}}$ partition coefficient of element between sulfide and silicate melt, $D_{\text{MSS/sulfide melt}}$ partition coefficient of element between MSS and sulfide melt; $C_{\text{sulfide melt}}$ initial concentration of element in sulfide melt, F remaining fraction of sulfide melt, C_L concentration of element in melt, C_S concentration of element in MSS

¹Barnes et al. (2013)

²Barnes and Ripley (2016)

³Mungall et al. (2005)

⁴Staude and Markl (2019)

⁵Liu and Brenan (2015)

⁶Barnes et al. (1997)

the thickest net-textured sulfides I. These data thus indicate that this area represents a relatively evolved melt pool and not an MSS cumulate.

Figure 13 highlights the compositional difference between the sulfides in the centre of Moran and those along the flanks and between the various types of net-textured sulfides (Fig. 13c, d). In the profile of drill hole MRDDH086, massive sulfides display a higher MSS content compared to net-textured sulfides I (as expressed by relatively high Os-Rh and relatively low Pt-Cu), whereas net-textured sulfides II exhibit an overall higher chalcophile element content. The higher chalcophile element content in net-textured ore layer II indicates that the new sulfide melt batch interacted with more komatiite melt, which is also evident in Fig. 11f, showing that data for the net-textured II sulfides are on average shifted more towards higher R factors compared to net-textured sulfide I.

There is no systematic vertical PGE tenor variation through the sulfide pool at any point; all of the variation is taking place from the edge of the sulfide pool (i.e. the pinchout) to the centre of the embayment, where the fractionated residuum is found. This observation suggests that the MSS cumulate accreted laterally inwards rather than from the floor upwards as conventionally assumed (Usselman et al. 1979) or from the top downwards as inferred for the

Silver Swan sulfide pool by Barnes (2004). The residual fractionated melt evidently migrated laterally inwards ahead of the crystallization front. This is a remarkable feature considering that the sulfide pool is a thin sheet-like body with a surface of about 600 m by 100 m and a thickness of only 0.2 to 4 m, raising the question of why the residual melt would migrate towards the centre of the pool rather than remaining trapped in interstitial space between cumulus MSS crystals. This process clearly could not have been driven by gravitational settling of cumulus crystals and implies that fractional crystallization must have involved in situ nucleation and the growth of MSS crystals from an advancing boundary layer.

This process of lateral fractionation may have an analogue in granitic pegmatite systems. Hydrous melts of granitic pegmatites have a very low viscosity (1–10 Pa s) (Bartels et al. 2013) similar to sulfide melts (10^{-3} – 10^{-2} Pa s) (Rose and Brenan 2001) and, similar to lava flows, crystallize quickly (within weeks) (London 2014). Based on experiments, London (2014) suggested that a low-viscosity compositional boundary layer liquid (the rejected solute) forms between the crystallized pegmatite and the crystallizing melt. The boundary layer retains the incompatible elements left behind after crystallization, and it migrates in the direction of the propagation of the crystallization front. Once this remaining melt crystallizes, it forms a sharp boundary

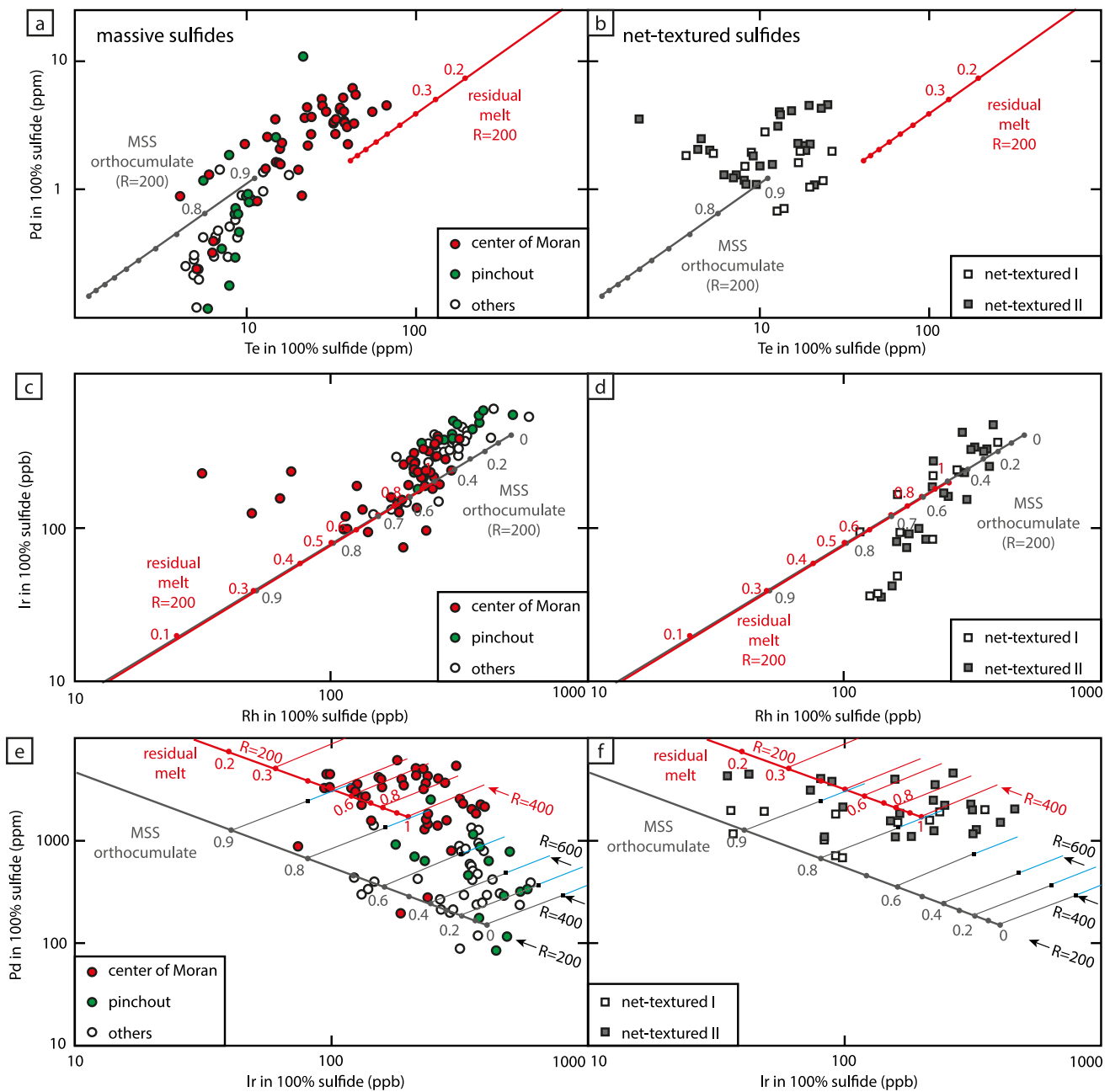


Fig. 11 Behaviour of trace elements during fractional crystallization of a sulfide melt with trends shown for MSS formation (black line) and remaining residual melt (red line) with numbers indicating the fraction of MSS and melt, respectively (Table 2). **a** Pd versus Te in massive sulfides and **b** in net-textured sulfides. **c** Ir versus Rh in mas-

sive sulfides and **d** in net-textured sulfides. **e** Pd versus Ir in massive sulfides and **f** in net-textured sulfides. In **e** and **f**, calculated behaviour of trace elements is shown for variable R factors. Colours for sulfide data are the same as in Figs. 1b and 6

to the initial pegmatite with exotic minerals formed by the incompatible elements. The Moran sulfide pool could have crystallized in a similar way despite the vastly different physical properties of the melt. Pinchout sulfides crystallized inward from the contact to the colder basalt and due to the pinchout geometry of basalt underneath and above, forming a crystallizing wall of MSS cumulate. Inward

propagation of the MSS-melt boundary layer caused this layer of residual melt to migrate laterally ahead of the crystallization front towards the centre of the pool (Fig. 14a–c). This model requires that the chemical diffusion is faster than thermal diffusion (Barnes and Robertson 2019). Manthilake et al. (2019) proposed a value of thermal diffusivity for pyrrhotite around $10^0 \text{ Wm}^{-1} \text{ K}^{-1}$ which results in a thermal

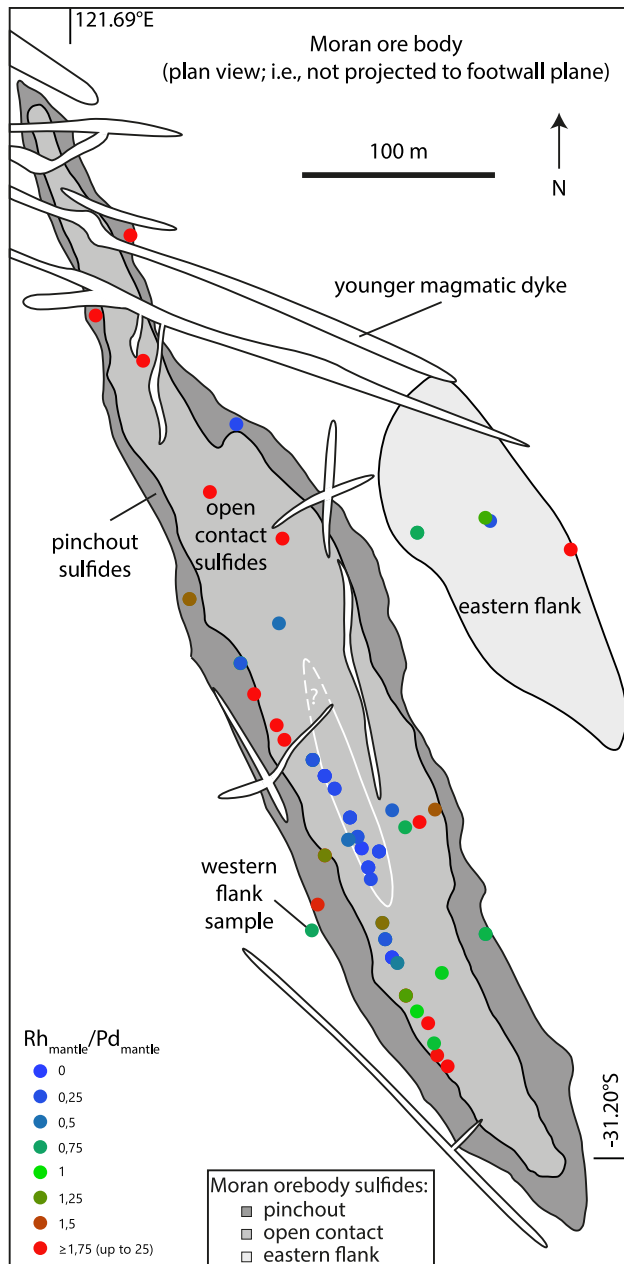


Fig. 12 Mantle-normalized Rh/Pd ratio of massive sulfides to show the distribution of high Rh/Pd which is interpreted to represent MSS cumulate. Note the low Rh/Pd in the centre of the deposit which represents the solidified residual sulfide melt, the end product of the inward fractional crystallization of the sulfide pool. The morphology of the residual melt pool (white line) resembles the geometry of the orebody and represents 15% of the surface area of the orebody or <1% of the original sulfide pool volume (see text). Primitive mantle composition was taken from McDonough and Sun (1995)

diffusion of $10^{-6} \text{ m}^2/\text{s}$ (Ashby 2011). Chemical diffusion in pyrrhotite was investigated for Fe (around 700 °C) and Os (950–1100 °C) and is in the order of 10^{-5} – $10^{-6} \text{ m}^2/\text{s}$ (Condit et al. 1974; Brenan et al. 2000; Cherniak 2010), which is similar to the thermal diffusion. A sulfide melt would have

an even faster chemical diffusion compared to solid pyrrhotite (as solids usually have lower diffusion rates than liquids) (Watson and Baxter 2007), and thus, it seems possible that the residual melt is able to migrate horizontally in front of the crystallizing MSS. The same mechanism of a compositional boundary layer could be responsible for the separation of Cu-rich orebodies frequently observed in mafic intrusion-associated deposits.

The boundary layer model can also explain the differences in sulfide chemistry between massive and net-textured sulfides. Net-textured sulfides in immediate contact with massive sulfides have usually a higher concentration of Pt, Pd and Au (ESM 4). This observation has also been reported in Kambalda from the Lunnon deposit by Keays et al. (1981) and from the Juan, Lunnon and Long deposits by Cowden et al. (1986), from Alexo (Canada) by Barnes and Naldrett (1986) and from Agnew (WA) by Barnes et al. (1988b). When the MSS crystallization front reaches the areas outside the pinchout, it coincides with the formation of net-textured sulfides (Fig. 14b), i.e. where olivine submerges into sulfides, and hence, sulfides are displaced upwards in the cumulate pile. The last formation of net-textured sulfides at any point in open contact position is when MSS forms underneath the submerging olivine. Hence, the last liquid sulfide during the formation of the net-texture is the fractionated residual melt of the boundary layer (Fig. 14b, c).

The sharp decrease of Co in pentlandite in the centre of Moran could indicate that another Co-bearing phase forms and scavenges the majority of Co from the remaining melt — prior to the formation of high-form pentlandite. This other Co-bearing phase could be Fe- and Ni-bearing cobaltite, which is much more abundant in the centre of Moran, although the Co tenor does not change.

Euhedral cobaltite generally overgrows euhedral spherulite and is overgrown by anhedral tellurides showing a common origin (Fig. 3b). In some mafic systems, fractional crystallization can lead to the formation of a late Pt-, Pd- and Au-bearing arsenide-telluride melt, which is immiscible with the sulfide melt (Helmy et al. 2007, 2010, 2013; Sinyakova and Kosyakov 2012; Bai et al. 2017). The concentration of As observed in the centre of Moran is about 100 times lower than necessary for an immiscible arsenide melt (0.5–1.5 wt%) (Helmy et al. 2013); however, that could be a fact of the sample size. As discussed above, the central area represents less than 1% of the initial sulfide melt pool. Taking a whole-rock sulfide sample, it could include pockets of 10 to 100 times higher fractionated melt compared to what the whole sample represents. For maximum contents of Te or Bi in sulfide melts, no data are available. The presence of composite grains in the centre of Moran, however, is a strong indication that an immiscible Pt–Pd–Co-bearing As–Te–Bi melt forms.

Fig. 13 Mantle-normalized spidergrams of chalcophile elements in 100% sulfides comparing **a** massive sulfides of the centre of the Moran deposit to massive sulfides on the flank, **b** massive sulfides of the centre to massive sulfides in the pinchout, **c** net-textured sulfide I to net-textured sulfide II and **d** massive sulfides to net-textured sulfides I and II of drill hole MRDDH086. Primitive mantle composition was taken from McDonough and Sun (1995)

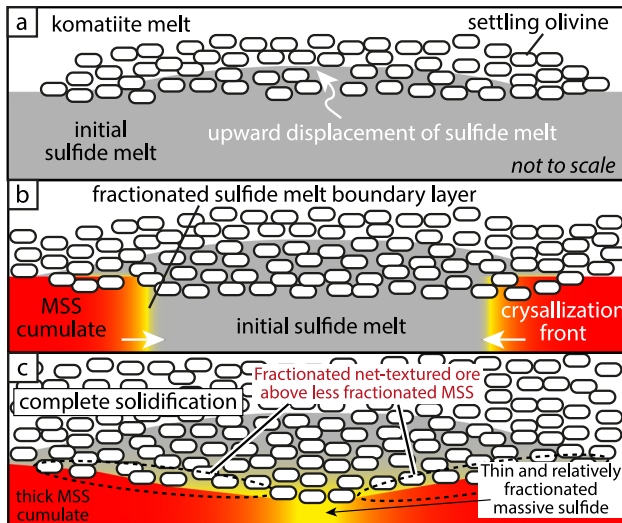
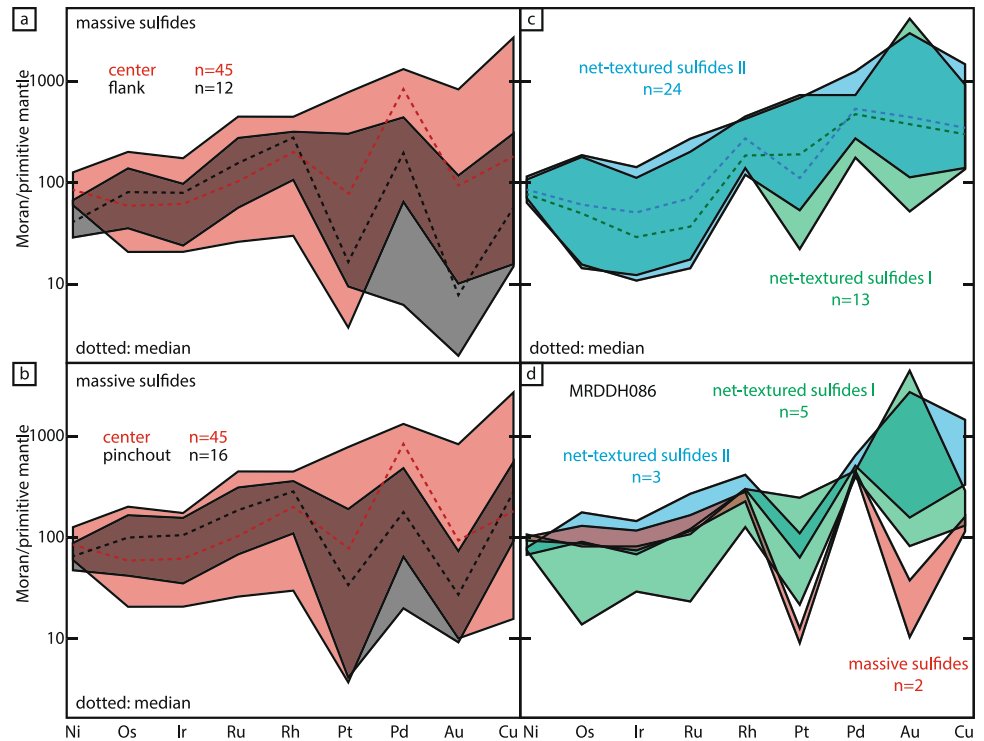


Fig. 14 Cartoon illustrating the crystallization of sulfides to explain the observed variations in major and trace elements. **a** Net-textured ore forms by partial sinking of olivine crystal pile into sulfide melt. **b** Once the sulfide liquidus is reached, MSS starts to crystallize (from the pinchout). On the contact to MSS, melt enriched in incompatible elements is concentrated forming a boundary layer. During progressive crystallization of MSS, the boundary layer migrates to the centre of the sulfide melt pool. **c** The boundary layer formation is the last process which coincides with the formation of net-textured ore as no further olivine can submerge after MSS formation. Therefore, net-textured ore on the contact to massive sulfides display the highest concentration of incompatible elements, whereas massive sulfides directly underneath display lower concentrations of incompatible elements

Conclusions

The komatiite-hosted Moran sulfide ores preserve the igneous textures and primary magmatic chemistry of major and trace elements despite upper greenschist facies metamorphism. This allows for a detailed assessment of the sulfide evolution through all stages of ore formation. Older sedimentary sulfides were entrained in the komatiite forming early low-Ni tenor sulfides in a concave embayment, now preserved on the flank of Moran. A second younger type of sulfide, with higher Ni tenor, is present in the steep-sided embayment (up to 40 m deep at its final position). This is formed due to thermomechanical erosion within the previous concave embayment. The final thermal erosion occurs sideways to form the pinchout that surrounds the entire orebody. When the komatiite eruption ceases, the whole system cools down, and olivine starts to settle forming net-textured sulfides in line with the classical “billiard ball model” (Naldrett 1973). Further cooling causes interstitial silicate melt to crystallize, arresting the formation of net-textured ore and creating a barren komatiite layer on top of the net-textured ore. A subsequent mush of flowing olivine-komatiite melt contains also sulfide melt and deposits it above the barren layer forming a second net-textured layer.

The sulfide melt pool underneath the net-textured ore crystallizes as a closed system. Elements compatible with regard to MSS show that the melt crystallizes and fractionates from the edge towards the centre. Thus, a new model of sulfide melt crystallization is proposed: a boundary

layer liquid, containing the incompatible elements, forms between the crystallizing MSS and the remaining melt in a similar way as it was proposed for crystallizing pegmatites (London 2014). This layer migrates in the direction of the propagating crystallization front. This model can potentially be applied to other magmatic sulfide deposits to explain the separation of Cu-rich sulfide melt from the Fe–Ni-rich portion of the sulfides.

In the centre of the orebody, the last highly fractionated melt crystallizes. These last sulfides represent less than 1% of the initial sulfide pool and contain composite Co- and Bi-bearing arsenide-telluride grains. A sharp decrease of Co in pentlandite in the same area, with a sharp increase in whole-rock As, Bi and Te, suggest that the composite grains form prior to pentlandite formation, possibly as immiscible As-Bi-Te melt.

Supplementary Information The online version contains supplementary material available at <https://doi.org/10.1007/s00126-021-01060-5>.

Acknowledgements We are grateful to IGO Limited, particularly Susan Leeson, Karly Ding, Mike Whitford and Shane Stanfield for their help with sampling. The funding of some of the whole-rock analysis by IGO is also gratefully acknowledged. SS is particularly grateful to Steve Barnes for the Maia Mapper images, for sharing information and for discussions from which the manuscript benefited greatly. Marcus Oelze acknowledges the financial support of the Helmholtz Recruitment Initiative to Sarah A. Gleeson. Sarah-Jane Barnes and Michael Leshner are thanked for the comments on an early version of the manuscript. Very detailed reviews by Marco L. Fiorentini and Michel G. Houlié, as well as from the editor Wolfgang D. Maier, improved the manuscript notably. Peter Simmonds is thanked for English proof-reading.

Funding The research was funded by the German Research Foundation (grant no. 407352165) to SS. Open Access funding enabled and organized by Projekt DEAL.

Open Access This article is licensed under a Creative Commons Attribution 4.0 International License, which permits use, sharing, adaptation, distribution and reproduction in any medium or format, as long as you give appropriate credit to the original author(s) and the source, provide a link to the Creative Commons licence, and indicate if changes were made. The images or other third party material in this article are included in the article's Creative Commons licence, unless indicated otherwise in a credit line to the material. If material is not included in the article's Creative Commons licence and your intended use is not permitted by statutory regulation or exceeds the permitted use, you will need to obtain permission directly from the copyright holder. To view a copy of this licence, visit <http://creativecommons.org/licenses/by/4.0/>.

References

- Ashby MF (2011) *Materials selection in mechanical design*. Elsevier, pp 646
- Bai I, Barnes SJ, Baker DR, (2017) Sperrylite saturation in magmatic sulfide melts: implications for formation of PGE-bearing arsenides and sulfarsenides. *Am Miner* 102:966–974
- Barnes SJ, Naldrett AJ (1986) Variations in platinum group element concentrations in the Alexo mine komatiite, Abitibi greenstone belt, northern Ontario. *Geol Mag* 123:515–524
- Barnes SJ, Ripley EM (2016) Highly siderophile and strongly chalcophile elements in magmatic ore deposits. *Rev Miner Geochem* 81:725–774
- Barnes SJ, Makovicky E, Makovicky M, Rose-Hansen J, Karup-Moller S (1997) Partition coefficients for Ni, Cu, Pd, Pt, Rh, and Ir between monosulfide solid solution and sulfide liquid and the formation of compositionally zoned Ni-Cu sulfide bodies by fractional crystallization of sulfide liquid. *Can J Earth Sci* 34:366–374
- Barnes Stephen J (2004) Komatiites and nickel sulfide ores of the Black Swan area, Yilgarn Craton, Western Australia. 4. Platinum group element distribution in the ores, and genetic implications. *Miner Depos* 39:752–765
- Barnes SJ (2006a) Komatiites: petrology, volcanology, metamorphism, and geochemistry. *Soc Econ Geol Spec Pub* 13:13–49
- Barnes SJ (2006b) Komatiite-hosted nickel sulfide deposits: geology, geochemistry, and genesis. *Soc Econ Geol Spec Pub* 13:51–118
- Barnes SJ, Liu W (2012) Pt and Pd mobility in hydrothermal fluids: evidence from komatiites and from thermodynamic modelling. *Ore Geol Rev* 44:49–58
- Barnes SJ, Robertson JC (2019) Time scales and length scales in magma flow pathways and the origin of magmatic Ni-Cu-PGE ore deposits. *Geosci Front* 10:77–87
- Barnes SJ, Gole MJ, Hill RET (1988a) The Agnew nickel deposit, Western Australia: part I. Stratigraphy and Structure *Econ Geol* 83:524–536
- Barnes SJ, Gole MJ, Hill RET (1988b) The Agnew nickel deposit, Western Australia: part II. Sulfide geochemistry, with emphasis on the platinum-group elements. *Econ Geol* 83:537–550
- Barnes SJ, Heggie GJ, Fiorentini ML (2013) Spatial variation in platinum group element concentrations in ore-bearing komatiite at the Long-Victor Deposits, Kambalda Dome, Western Australia: enlarging the footprint of nickel sulfide orebodies. *Econ Geol* 108:913–933
- Barnes SJ, Mungall JE, Le Vaillant M, Godel B, Leshner CM, Holwell D, Lightfoot PC, Krivolutskaia N, Wei B (2017) Sulfide-silicate textures in magmatic Ni-Cu-PGE sulfide ore deposits: disseminated and net-textured ores. *Am Mineral* 102:473–506
- Barnes SJ, Staude S, Le Vaillant M, Piña R, Lightfoot PC (2018) Sulfide-silicate textures in magmatic Ni-Cu-PGE sulfide ore deposits: massive, semi-massive and sulfide-matrix breccia ores. *Ore Geol Rev* 101:629–651
- Barnes SJ, Taranovic V, Schoneveld LE, Mansur E, Le Vaillant M, Dare S, Staude S, Evans NJ, Blanks D (2020) The occurrence and origin of pentlandite-chalcopyrite-pyrrhotite loop textures in magmatic Ni-Cu sulfide ores. *Econ Geol* 115:1777–1798
- Bartels A, Behrens H, Holtz F, Schidt BC, Fechtelkorn M, Knipping J, Crede L, Baasner A, Pukallus N (2013) The effect of fluorine, boron and phosphorus on the viscosity of pegmatite forming melts. *Chem Geol* 346:184–198
- Bavinton OA (1981) The nature of sulfidic metasediments at Kambalda and their broad relationships with associated ultramafic rocks and nickel ores. *Econ Geol* 76:1606–1628
- Beresford SW, Cas RAF (2001) Komatiitic invasive lava flows, Kambalda, Western Australia. *Can Miner* 39:525–535
- Brenan JM, Cherniak DJ, Rose L (2000) Diffusion of osmium in pyrrhotite and pyrite: implications for closure of the Re-Os isotopic system. *Earth Planet Sci Lett* 180:399–413
- Brenner TL, Teixeira NA, Oliveira JAL, Franke ND, Thompson JFH (1990) The O’Toole nickel deposit, Morro do Ferro Greenstone Belt, Brazil. *Econ Geol* 85:904–920
- Brown MAN, Jolly RJH, Stone W, Coward MP (1999) Nickel ore troughs in Archaean volcanic rocks, Kambalda, Western Australia: indicators of early extension. *Geol Soc Spec Publ* 155:197–211

- Cherniak DJ (2010) Diffusion in carbonates, fluorite, sulfide minerals, and diamonds. *Rev Mineral Geochem* 72:871–897
- Condit RH, Hobbins RR, Birchenall CE (1974) Self-diffusion of iron and sulfur in ferrous sulfide. *Oxid Met* 8:409–455
- Cowden A, Donaldson MJ, Naldrett AJ, Campbell IH (1986) Platinum-group elements and gold in the komatiite-hosted Fe-Ni-Cu sulfide deposits at Kambalda, Western Australia. *Econ Geol* 81:1226–1235
- Dare SAS, Sarah-J B, Prichard HM, Fisher PC (2014) Mineralogy and geochemistry of Cu-rich ores from the McCreedy East Ni-Cu-PGE deposit (Sudbury, Canada): implications for the behaviour of platinum group elements at the end of crystallization of a sulfide liquid. *Econ Geol* 109:343–366
- Duran CJ, Sarah-J B, Pleše P, Kudrna Prašek M, Zientek ML, Pagé P (2017) Fractional crystallization-induced variations in sulfides from the Noril'sk-Talnakh mining district (polar Siberia, Russia). *Ore Geol Rev* 90:326–351
- Ewers WE, Hudson DR (1972) An interpretive study of a nickel-iron sulfide ore intersection, Lunnon Shoot, Kambalda, Western Australia. *Econ Geol* 67:1075–1092
- Garuti G, Rinaldi R (1986) Mineralogy of melonite-group and other tellurides from the Ivrea-Verbanò Basic Complex, western Italian Alps. *Econ Geol* 81:1213–1217
- Gole MJ, Barnes SJ (2020) The association between Ni-Cu-PGE sulfide and Ni-Co lateritic ores and volcanic facies within the komatiites of the 2.7 Ga East Yilgarn Craton Large Igneous Province, Western Australia. *Ore Geol Rev* 116:103231
- Goscombe B, Blewett RS, Czarnota K, Groenwald PB, Maas R (2009) Metamorphic evolution and integrated terrane analysis of the Eastern Yilgarn Craton: rationale, methods, outcomes and interpretation. *Geosci Aust Rec* 2009:23
- Gresham JJ, Loftus-Hills GD (1981) The geology of the Kambalda nickel field, Western Australia. *Econ Geol* 76:1373–1416
- Groves DI, Barrett FM, Binns RA, McQueen KG (1977) Spinel phases associated with metamorphosed volcanic-type iron-nickel sulfide ores from Western Australia. *Econ Geol* 72:1224–1244
- Groves DI, Korkiakoski EA, McNaughton NJ, Leshner CM, Cowden A (1986) Thermal erosion by komatiites at Kambalda, Western Australia and the genesis of nickel ores. *Nat* 319:136–139
- Heath C, Lahaye Y, Stone WE, Lambert DD (2001) Origin of variations in nickel tenor along the strike of the Edwards Lode nickel sulfide orebody, Kambalda, Western Australia. *Can Mineral* 39:655–671
- Helmy HM, Ballhaus C, Berndt J, Bockrath C, Wohlgenuth-Ueberwasser C (2007) Formation of Pt, Pd and Ni tellurides: experiments in sulfide-telluride systems. *Contrib Mineral Petrol* 153:577–591
- Helmy HM, Ballhaus C, Wohlgenuth-Ueberwasser C, Fonseca ROC, Laurenz V (2010) Partitioning of Se, As, Sb, Te and Bi between monosulfide solid solution and sulfide melt – application to magmatic sulfide deposits. *Geochim Cosmochim Acta* 74:6174–6179
- Helmy HM, Ballhaus C, Fonseca ROC, Nagel TJ (2013) Fractionation of platinum, palladium, nickel, and copper in sulfide-arsenide systems at magmatic temperature. *Contrib Mineral Petrol* 166:1725–1737
- Houlé MG, Leshner CM, Davis PC (2012) Thermomechanical erosion at the Alexo Mine, Abitibi greenstone belt, Ontario: implications for the genesis of komatiite-associated Ni–Cu–(PGE) mineralization. *Miner Deposita* 47:105–128
- Hronsky JMA, Schodde RC (2006) Nickel exploration history of the Yilgarn Craton: from the nickel boom to today. *Soc Econ Geol Spec Pub* 13:1–11
- Huppert HE, Sparks RSJ (1985) Komatiites I: eruption and flow. *J Petrol* 26:694–725
- Járóka T, Staude S, Seifert T, Pfänder JA, Bauer ME, Krause J, Schulz B (2021) Mineralogical and geochemical constraints on the origin of the Sohland-Rožany Ni-Cu-(PGE) sulfide mineralization (Lausitz Block, Bohemian Massif, Germany/Czech Republic). *Ore Geol Rev* 133:104055
- Keays RR, Ross JR, Woolrich P (1981) Precious metals in volcanic peridotite-associated nickel sulfide deposits in Western Australia. II: distribution within the ores and host rocks at Kambalda. *Econ Geol* 76:1645–1674
- Kirkham R, Dunn PA, Kuczewski AJ, Siddons DP, Dodanwala R, Moorhead GF, Ryan CG, De Geronimo G, Beuttenmuller R, Pinelli D, Pfeffer M, Davey P, Jensen M, Paterson DJ, de Jonge MD, Howard DL, Küsel M, McKinlay J (2010) The Maia spectroscopy detector system: engineering for integrated pulse capture, low-latency scanning and real-time processing. *AIP Conf Proc* 1234:240–243
- Kiseeva ES, Wood BJ (2015) The effects of composition and temperature on chalcophile and lithophile element partitioning into magmatic sulphides. *Earth Planet Sci Lett* 424:280–294
- Kitakaze A, Machida T, Komatsu R (2016) Phase relations in the Fe-Ni-S system from 875 to 650 °C. *Can Miner* 54:1175–1186
- Leshner CM (1989) Komatiite-associated nickel sulfide deposits. *Rev Econ Geol* 4:45–101
- Leshner CM (2007) Ni–Cu–(PGE) Deposits in the Raglan area, Cape Smith Belt, New Quebec. In: Goodfellow WD (ed) Mineral deposits of Canada: a synthesis of mineral deposit-types, district metallogeny, the evolution of geological provinces, and exploration methods. Mineral Deposits Division, Geological Association of Canada, special publication 5. Mineral Deposits Division, Geological Association of Canada, St John's, pp 351–386
- Leshner CM, Campbell IH (1993) Geochemical and fluid dynamic modeling of compositional variations in Archean komatiite-hosted nickel sulfide ores in Western Australia. *Econ Geol* 88:804–816
- Leshner CM, Burnham OM (2001) Multicomponent elemental and isotopic mixing in Ni-Cu-(PGE) ores at Kambalda, Western Australia. *Can Mineral* 39:421–446
- Leshner CM, Arndt NT, Groves DI (1984) Genesis of komatiite-associated nickel sulphide deposits at Kambalda, Western Australia: a distal volcanic model. In: Buchanan DL, Jones MJ (eds) Sulphide deposits in mafic and ultramafic rocks. Institute of Mining and Metallurgy, London, pp 70–80
- Leshner CM, Burnham OM, Keays RR, Barnes Stephen J, Hulbert L (2001) Trace-element geochemistry and petrogenesis of barren and ore-associated komatiites. *Can Mineral* 39:673–696
- Le Vaillant M, Barnes Stephen J, Fiorentini ML, Sarah-J B, Bath A, Miller J (2018) Platinum-group element and gold contents of arsenide and sulfarsenide minerals associated with Ni and Au deposits in Archean greenstone belts. *Mineral Mag* 82:625–647
- Lightfoot PC (2017) Nickel sulfide ores and impact melts. Elsevier
- Lightfoot PC, Stewart R, Gribbin G, Mooney SJ (2017) Relative contribution of magmatic and post-magmatic processes in the genesis of the Thompson Mine Ni-Co sulfide ores, Manitoba, Canada. *Ore Geol Rev* 83:258–286
- Liu Y, Brennan J (2015) Partitioning of platinum-group elements (PGE) and chalcogens (Se, Te, As, Sb, Bi) between monosulfide-solid solution (MSS), intermediate solid solution (ISS) and a sulfide liquid at controlled fO₂-fS₂ conditions. *Geochim Cosmochim Acta* 159:139–161
- London D (2014) A petrologic assessment of internal zonation in granitic pegmatites. *Lithos* 174–187:74–104
- Mansur ET, Sarah-J B, Duran CJ (2019) Textural and compositional evidence for the formation of pentlandite via peritectic reaction: implications for the distribution of highly siderophile elements. *Geol* 47:351–354
- Mansur ET, Barnes SJ, Duran CJ, Sluzhenikin SF (2020) Distribution of chalcophile and platinum-group elements among pyrrhotite, pentlandite, chalcopyrite and cubanite from the Noril'sk-Talnakh ores: implications for the formation of platinum-group minerals. *Miner Deposita* 55:1215–1232
- Manthilake G, Chantel J, Monteux J, Andrault D, Bouhifd MA, Bolfan Casanova N, Boulard E, Guignot N, King A, Itie JP (2019) Thermal conductivity of FeS and its implications for Mercury's long-sustaining magnetic field. *J Geophys Res: Planet* 124:2359–2368

- Mao X, Li L, Liu Z, Zeng R, Dick JM, Yue B, Ai Q (2019) Multiple magma conduits model of the Jinchuan Ni-Cu-(PGE) deposit, northwestern China: constraints from the geochemistry of platinum-group elements. *Minerals* 9:187
- McDonough WF, Sun SS (1995) The composition of the Earth. *Chem Geol* 120:223–253
- Mungall JE, Andrews DRA, Cabri LJ, Sylvester PJ, Tubrett M (2005) Partitioning of Cu, Ni, Au, and platinum-group elements between monosulfide solid solution and sulfide melt under controlled oxygen and sulfur fugacities. *Geochim Cosmochim Acta* 69:4349–4360
- Naldrett AJ (1973) Nickel sulphide deposits – their classification and genesis, with special emphasis on deposits of volcanic association. *Can Inst Mining Met Trans* 76:183–201
- Naldrett AJ (2004) Magmatic sulfide deposits. Springer
- Naldrett AJ (2010) Secular variation of magmatic sulfide deposits and their source magmas. *Econ Geol* 105:669–688
- Naldrett AJ, Fedorenko VA, Asif M, Shushen L, Kunilov VE, Stekhin AI, Lightfoot PC, Gorbachev NS (1996) Controls on the composition of the Ni-Cu sulfide deposits as illustrated by those at Noril'sk, Siberia. *Econ Geol* 91:751–773
- Paton C, Hellstrom J, Paul B, Woodhead J, Hergt J (2011) Iolite: freeware for the visualisation and processing of mass spectrometric data. *J Anal at Spectrom* 26:2508–2511
- Perring CS (2015) Volcanological and structural controls on mineralization at the Mount Keith and Cliffs komatiite-associated nickel sulfide deposits, Agnew-Wiluna belt, Western Australia-implications for ore genesis and targeting. *Econ Geol* 110:1669–1695
- Piispanen R, Tarkian M (1984) Cu-Ni-PGE mineralization at Rometölvas, Koillismaa layered igneous complex, Finland. *Mineral Deposita* 19:105–111
- Robertson JC, Kerr RC (2012) Solidification dynamics in channeled viscoplastic lava flows. *J Geophys Res* 117, Citation B07206
- Rose LA, Brenan JM (2001) Wetting properties of Fe-Ni-Co-Cu-O-S melts against olivine: implications for sulfide melt mobility. *Econ Geol* 96:145–157
- Ryan CG, Siddons DP, Kirkham R, Li ZY, de Jonge MD, Paterson DJ, Kuczewski A, Howard DL, Dunn PA, Falkenberg G, Boesenberg U, De Geronimo G, Fisher LA, Halfpenny A, Lintern MJ, Lombi E, Dyl KA, Jensen M, Moorhead GF, Cleverly JS, Hough RM, Godel B, Barnes Stephen J, James SA, Spiers KM, Alfeld M, Wellenreuther G, Vukmanovic Z, Borg S (2014) Maia X-ray fluorescence imaging: capturing detail in complex natural samples. *J Phys Conf Ser* 499:012002
- Ryan CG, Kirkham R, Moorhead G, Parry D, Jensen M, Faulks A, Hogan S, Dunn P, Dodanwala R, Fisher L, Pearce LA, Siddons DP, Kuczewski A, Lundström U, Trolliet A, Gao N (2018) Maia Mapper: high definition XRF imaging in the lab. *J Instrum* 13:C03020
- Said N, Kerrich R (2010) Elemental and Nd-isotope systematics of the Upper Basalt Unit, 2.7 Ga Kambalda Sequence: quantitative modeling of progressive crustal contamination of plume asthenosphere. *Chem Geol* 273:193–211
- Seat Z, Stone WE, Mapleson DB, Daddow BC (2004) Tenor variation within komatiite-associated nickel sulphide deposits: insights from the Wannaway deposit, Widgiemooltha Dome, Western Australia. *Mineral Petrol* 82:317–339
- Sinyakova EF, Kosyakov VI (2012) The behaviour of noble-metal admixtures during fractional crystallization of As- and Co-containing Cu-Fe-Ni sulfide melts. *Russian Geol Geophys* 53:1055–1076
- Squire RJ, Cas RAF, Clout JMF, Behets R (1998) Volcanology of the Archaean Lunnon Basalt and its relevance to nickel sulfide-bearing trough structures at Kambalda, Western Australia. *Aust J Earth Sci* 45:695–715
- Staude S, Markl G (2019) Remnant lenses of komatiitic dykes in Kambalda (Western Australia): occurrences, textural variations, emplacement model, and implications for other komatiite provinces. *Lithos* 342–343:206–222
- Staude S, Barnes Stephen J, Le Vaillant M (2016) Evidence of lateral thermomechanical erosion of basalt by Fe-Ni-Cu sulfide melt at Kambalda, Western Australia. *Geol* 44:1047–1050
- Staude S, Barnes Stephen J, Le Vaillant M (2017a) Thermomechanical erosion of ore-hosting embayments beneath komatiite lava channels: textural evidence from Kambalda, Western Australia. *Ore Geol Rev* 90:446–464
- Staude S, Sheppard S, Parker P, Paggi J (2017b) Long-Victor nickel sulfide deposits, Kambalda. In: Philips N (ed) *Australian Ore Deposits Monograph 32*. Australasian Institute of Mining and Metallurgy, Melbourne, pp 107–112
- Staude S, Jones TJ, Markl G (2020) The textures, formation and dynamics of rare high-MgO komatiite pillow lavas. *Precambrian Res* 343:105729
- Staude S, Barnes Stephen J, Markl G (2021) Interspinifex Ni sulfide ore from Victor South-McLeay: evidence for post-ore formation. *Miner Depos* 56:125–142
- Stone WE, Archibald NJ (2004) Structural controls on nickel sulphide ore shoots in Archaean komatiite, Kambalda, WA: the volcanic trough controversy revisited. *J Struct Geol* 26:1173–1194
- Stone WE, Beresford SW, Archibald NJ (2005) Structural setting and shape analysis of nickel sulfide shoots at the Kambalda Dome, Western Australia: implications for deformation and remobilization. *Econ Geol* 100:1441–1455
- Sylvester P (2001) Laser-ablation-ICPMS in the Earth sciences. Principles and applications. *Mineral Assoc Canada* 243
- Thomson B (1989) Petrology and stratigraphy of some texturally well preserved thin komatiites from Kambalda, Western Australia. *Geol Mag* 126:249–261
- Tolstykh ND, Krivolutsкая NA, Safonova MO, Shapovalova IY, Zhitova LM, Abersteiner A (2020) Unique Cu-rich sulphide ores of the Southern-2 orebody in the Talnakh Intrusion, Noril'sk area (Russia): geochemistry, mineralogy and conditions of crystallization. *Ore Geol Rev* 103525
- Usselman TM, Hogde DS, Naldrett AJ, Campbell IH (1979) Physical constraints on the characteristics of nickel-sulfide ore in ultramafic lavas. *Can Miner* 17:361–372
- Watson EB, Baxter EF (2007) Diffusion in solid-Earth systems. *Earth Planet Sci Lett* 253:307–327
- Williams DA, Kerr RC, Leshner CM (1998) Emplacement and erosion by Archean komatiite lava flows at Kambalda: revisited. *J Geophys Res Solid Earth* 103:27533–27549
- Wilson SA, Ridley WI, Koenig AE (2002) Development of sulfide calibration standards for the laser ablation inductively-coupled plasma mass spectrometry technique. *J Anal at Spectrom* 17:406–409
- Wohlge-muth-Ueberwasser CC, Ballhaus C, Berndt J, Stotter née Paliulionyte V, Meisel T (2007) Synthesis of PGE sulfide standards for laser ablation inductively coupled plasma mass spectrometry (LA-ICP-MS). *Contrib Miner Petrol* 154:607–617

Publisher's Note Springer Nature remains neutral with regard to jurisdictional claims in published maps and institutional affiliations.